Dynamical mean-field theory for Rényi entanglement entropy and mutual information in the Hubbard model

Surajit Bera,[1,*] Arijit Haldar,[2,3,†] and Sumilan Banerjee[1,‡]

[1]*Centre for Condensed Matter Theory, Department of Physics, Indian Institute of Science, Bangalore 560012, India*
[2]*S. N. Bose National Centre for Basic Sciences JD Block, Sector-III, Salt Lake City, Kolkata - 700 106, India*
[3]*Department of Physics, University of Toronto, 60 St. George Street, Toronto, Ontario, M5S 1A7, Canada*

(Received 1 April 2023; revised 4 January 2024; accepted 8 January 2024; published 24 January 2024)

Quantum entanglement, lacking any classical counterpart, provides a fundamental new route to characterize the quantum nature of many-body states. In this work, we discuss an implementation of a new path integral method [Phys. Rev. Res. **2**, 033505 (2020)] for fermions to compute entanglement for extended subsystems in the Hubbard model within dynamical mean-field theory (DMFT) in one and two dimensions. The new path integral formulation measures entanglement by applying a "kick" to the underlying interacting fermions. We show that the Rényi entanglement entropy can be extracted efficiently within the DMFT framework by integrating over the strength of the kick term. Using this method, we compute the second Rényi entropy as a function of subsystem size for metallic and Mott insulating phases of the Hubbard model. We explore the thermal entropy to entanglement crossover in the subsystem Rényi entropy in the correlated metallic phase. We show that the subsystem-size scaling of the second Rényi entropy is well described by the crossover formula which interpolates between the volume-law thermal Rényi entropy and the universal boundary-law Rényi entanglement entropy with logarithmic violation, as predicted by conformal field theory. We also study the mutual information across the Mott metal-insulator transition.

DOI: 10.1103/PhysRevB.109.035156

I. INTRODUCTION

Entanglement, arguably the strangest aspect of quantum mechanics, signifies the existence of true nonlocal quantum correlations. As a result, it has found enormous applications for characterizing quantum many-body states in condensed matter and high-energy physics, and as a resource for quantum computation [1]. In condensed matter systems, entanglement can be used to distinguish various kinds of symmetry-broken and topological states, gapped or gapless phases [2], etc. For instance, entanglement provides an unambiguous indicator of topological order [3,4] in quantum ground states. Entanglement has also emerged as an important measure for distinguishing high-energy states as well as nonequilibrium dynamics. For example, entanglement can be used to classify dynamical phases of isolated quantum systems as ergodic or many-body localized [5–7].

Entanglement of a quantum system is quantified in terms of various measures, e.g., von Neumann and Rényi entanglement entropies, mutual information and entanglement negativity [2,8,9]. These measures can be calculated by partitioning the overall system into two subsystems and computing the reduced density matrix of one of the subsystems by tracing over the other. To this end, the dependence of entanglement entropy on the size and geometry of the subsystem under various partitioning of the system are used to classify quantum many-body states and their nonlocal entanglement properties. For example, ground-states of gapped bosonic and fermionic systems in d dimensions follow the so-called "area law" or "boundary law" for entanglement entropy ($\sim L^{d-1}$) of a subsystem with length L [2,8,10,11]. In contrast, critical states in one dimension (1d) and fermionic systems with Fermi surface, i.e., standard metals, in any dimension exhibit a logarithmic violation [2,12–18] of the area law, namely, the subsystem entanglement entropy scales as $L^{d-1}\ln L$. These characterizations of the many-body ground states are mainly obtained through powerful analytical results based on conformal field theory (CFT) methods [8,19] and related arguments [15–18], as well as numerical results for noninteracting systems [11,14]. For the latter, entanglement measures can be computed efficiently using the correlation matrix of the subsystem [11]. However, numerical computations of entanglement entropy is much more challenging for interacting systems, typically limited to small systems accessible via exact diagonalization (ED) or 1d systems through density matrix renormalization group (DMRG) or heavily numerical and sophisticated quantum Monte Carlo (QMC) techniques [20–27].

The above numerical methods have provided many useful insights into entanglement characteristics of interacting systems. However, there is a lack of complementary quantum many-body methods, e.g., mean-field theories, perturbation expansions, and other approximations, for computing entanglement entropy of interacting systems, unlike those for usual thermodynamic, spectroscopic and transport properties.

*surajit@iisc.ac.in
†arijit.haldar@bose.res.in
‡sumilan@iisc.ac.in

The CFT techniques employ a replica path integral approach [8,19] where bosonic and fermionic fields are defined on a nontrivial space-time manifold with complicated boundary conditions. The latter are often hard to implement within the standard quantum many-body methodology, though important progress has been made for large-N models [28–32]. To circumvent this difficulty, a new path integral approach was first developed in Ref. [33] for bosons. It was subsequently extended to fermionic systems [34,35] as well as interacting bosons [36]. In particular, Ref. [34] employed this method to compute Rényi entanglement entropy of Fermi and non-Fermi liquid states of strongly interacting fermions described by Sachdev-Ye-Kitaev (SYK) and related models. The new method [34] replaces the complicated boundary conditions in the replica field theory for entanglement [8] by a fermionic self-energy that acts as a nonequilibrium kick. Using this new path integral formalism, here we develop a dynamical mean-field theory (DMFT) for Rènyi entanglement entropy in the paradigmatic Hubbard model [37–39] of strongly correlated electrons.

In the last three decades, single-site DMFT approximation and its cluster extensions [40,41], have gained popularity as a very successful approach to describe Mott metal-insulator transition and other associated electronic strong correlation phenomena, both in and out of equilibrium [42]. Integrating DMFT with first-principle electronic structure methods, like density functional theory (DFT), has provided a viable route to compute and predict properties of strongly correlated materials [41]. In the DMFT formulation, the strongly correlated lattice problem is reduced to a problem of a single impurity or cluster of sites coupled to a self-consistent bath [40]. The original single-site implementation of DMFT neglects spatial correlations but captures nontrivial local dynamical quantum correlations and becomes exact in infinite dimension $d \to \infty$ [40]. The later cluster extensions of DMFT [41,43–45], along with state-of-the-art impurity solver like continuous-time quantum Monte Carlo (CTQMC), incorporates back some of the spatial correlations, and can even provide a good description of the properties of one-dimensional systems [41,46,47].

In this work, we compute entanglement properties of the correlated metallic and insulating phases across the Mott metal-insulator transition in the Hubbard model. We use the cavity method [40] for the entanglement path integral of Ref. [34] to derive single-site DMFT self-consistency equations for obtaining the second Rényi entropy $S_A^{(2)}$ of a contiguous subsystem A. We show that the Rényi entropy can be extracted by integrating over the strength of a nonequilibrium "kick" perturbation acting on the imaginary-time evolution. Remarkably, this only requires the knowledge of onsite single-particle Green's function for the subsystem, even in the interacting system, albeit in the presence of the kick. Due to the entanglement cut(s) and the nonequilibrium kick, both the lattice and time translation symmetry are broken in the entanglement path integral. Thus the single-site DMFT is implemented as an inhomogeneous nonequilibrium DMFT. To this end, we develop an efficient recursive Green's function method to solve the DMFT self-consistency equations. Given the computational complexity of the problem, we only consider the Hubbard model at half filling and employ a simple DMFT impurity solver, namely the iterative perturbation theory (IPT). The latter is known to work very well when compared to more accurate exact diagonalization and QMC impurity solvers for the half-filled Hubbard model in equilibrium [40]. Our DMFT formulation is general and can be extended in future to incorporate cluster generalizations of DMFT [41,43–45] and more accurate impurity solvers, e.g., CTQMC [48].

Using the inhomogeneous nonequilibrium single-site DMFT for subsystem Rényi entropy, we compute $S_A^{(2)}$ in the Hubbard model as a function of temperature T, interaction U, and linear size of the subsystem N_A in 1d, and for 2d cylindrical subsystem geometry. In particular, we ask how the entanglement properties of correlated metal described by completely local self-energy approximation within single-site DMFT compare with those expected from CFT [8,12,19] and related arguments [15–18]. At high temperature, subsystem Rényi entropy $S_A^{(2)}$ is dominated by thermal entropy and, at low temperature, by entanglement [8,12,18,19,49]. We indeed find a crossover from thermal to entanglement behavior in $S_A^{(2)}$. Specifically, we find that this crossover in DMFT metallic state in 1d is well described by the known CFT crossover formula [8,12,49]. Moreover, one of our main results is to show that the ground-state entanglement entropy of metallic state in 2d Hubbard model within DMFT is consistent with a $\sim L \ln L$ subsystem-size scaling, i.e., logarithmic violation of the area law. The latter has been conjectured based on general arguments [15–18], results for noninteracting fermions [14], and other approximation [50]. We also compare our results for $S_A^{(2)}(N_A, T)$ with that available from QMC [24].

As a measure of entanglement at finite temperature [51], we extract Rényi mutual information between the subsystem A and the rest of the system from $S_A^{(2)}(N_A)$. We find that the mutual information has a hysteresis across the first-order Mott metal-insulator transition [40] in the U-T plane, culminating at the critical point where the transition becomes second order. There have been previous studies [52–55] of von Neumann entropy, mutual information as well as entanglement spectrum of a single site, or a few sites within a cluster, via cellular DMFT (CDMFT). Such *local* entanglement measures can be computed within the usual equilibrium DMFT formulation. However, the full subsystem size dependence of the entanglement entropy and mutual information cannot be obtained through such equilibrium DMFT. On the contrary, the general method we develop here can be applied for extended subsystems of arbitrary size and shape and requires an entirely different implementation through the new path integral technique [34] and nonequilibrium kick term.

Overall, the main goal of our work is to develop a practical method to compute entanglement properties of strongly correlated system, especially in two and higher dimension, analogous to usual equilibrium and nonequilibrium DMFT [40–42] for calculating thermodynamic, transport, spectral and out-of-equilibrium properties of strongly correlated materials. As a *proof of principle* and easier numerical demonstration, we first implement the method for 1d Hubbard model. However, we do not expect a mean-field approximation like single-site DMFT, which is based on infinite-dimensional local self-energy approximation [40], to be even qualitatively correct in 1d. Using the new method we obtain some

important results on entanglement properties of strongly correlated metal in 2d Hubbard model, e.g, the entanglement to thermal crossover in the correlated metallic state and mutual information of extended subsystem across Mott metal-insulator transition. DMFT is typically known to provide a good description of properties of strongly correlated 3d systems. The approximation is less accurate in 2d. Nevertheless, DMFT has been applied to describe many correlated phenomena in 2d, e.g., see Refs. [56–59].

The rest of the paper is organized as follows. We discuss the mathematical foundations of the path integral formulation in Sec. II. In Sec. III, we briefly revise the general path integral formalism of Ref. [34] for the second Rényi entropy and discuss how the Rényi entropy can be extracted by integrating over the strength of a nonequilibrium kick term. The DMFT approximation for the entanglement path integral is discussed in Sec. IV in the context of half-filled Hubbard model. The numerical solution of the DMFT self-consistency equations and benchmarks performed using the noninteracting limit and previous QMC simulations are discussed in Sec. V. We then discuss our main results for the subsystem size dependence of Rényi entropy in 1d and 2d Hubbard model and the thermal entropy to entanglement crossover in Secs. VI and VII. In Sec. VIII, we discuss the mutual information across the Mott metal-insulator transition. We summarize our results and discuss the scope of our work and possible future extensions in Sec. IX. The details of the numerical implementations of the DMFT equations, benchmarks, analysis of the results and an extension to incorporate magnetic order are given in Appendixes A–I.

II. THE PATH INTEGRAL FOR SUBSYSTEM RÉNYI ENTROPY

The coherent state path integral approach to subsystem Rényi entropy is comprehensively discussed in Ref. [34]. In this section, we provide a concise overview of the fundamental steps for setting up the path integral formalism for completeness. To compute the subsystem Rényi entropy of a given quantum state represented by the density matrix ρ, the system is divided into two parts, A and B. Then the reduced density matrix for A is obtained by tracing out the degrees of freedom in B, as $\rho_A = \mathrm{Tr}_B(\rho)$. Subsequently, the nth Rényi entropy for the subsystem A is calculated from

$$S_A^{(n)} = \frac{1}{1-n} \ln \mathrm{Tr}_A\left[\rho_A^n\right]. \tag{1}$$

The primary challenge in evaluating the above arises from the representation of $\mathrm{Tr}_A[\rho_A^n] = \mathrm{Tr}_A[(\mathrm{Tr}_B\rho)(\mathrm{Tr}_B\rho)\ldots(\mathrm{Tr}_B\rho)]$ within a coherent-state path integral framework [8]. Each instances of $\mathrm{Tr}_B\rho$ above generates distinct replicas that must be linked with suitable boundary conditions when expressed in the coherent-state basis, leading to a path integral on a complicated path-integral manifold, namely an n-sheeted Riemann surface [8].

To overcome the above challenge, we derive an operator expansion [34] (see Appendix A of Ref. [34])

$$F = \int d^2\xi f(\xi_1,\xi_2)\mathrm{Tr}_A[FD(\xi_2)]D(\xi_1), \tag{2}$$

where $F = F(\{c^\dagger_{i\in A}, c_{i\in A}\})$ is an arbitrary operator with support only in the A subsystem, such that F can be represented in terms of only local fermionic operators $\{c_i^\dagger, c_i\}$ in A; $i = 1,\ldots,N_A$ can denote site and/or spin index in A and the trace Tr_A only acts on A. In Eq. (2), instead of expansion in the coherent state basis, F has been expanded in the basis of normal-ordered *fermionic* displacement operators [60]

$$D(\xi_\alpha) = e^{\sum_{i\in A} c_i^\dagger \xi_{i\alpha}} e^{-\sum_{i\in A}\bar{\xi}_{i\alpha}c_i}, \quad \alpha = 1,2, \tag{3}$$

where $\bar{\xi}_{i\alpha}$, $\xi_{i\alpha}$ are static auxiliary Grassmann fields with $d^2\xi = \prod_{i\in A,\alpha} d\bar{\xi}_{i\alpha}d\xi_{i\alpha}$, and

$$f(\xi_1,\xi_2) = 2^{N_A} e^{-\frac{1}{2}\sum_{i\in A}(\bar{\xi}_{i1}\xi_{i1}+\bar{\xi}_{i2}\xi_{i2}-\bar{\xi}_{i1}\xi_{i2}+\bar{\xi}_{i2}\xi_{i1})} \tag{4}$$

is a Gaussian factor connecting two replicas $\alpha = 1, 2$. Using Eq. (2), we can write down the trace of product of two operators F and G in A as

$$\mathrm{Tr}_A[FG] = \int d^2\xi f(\xi_2,\xi_1)\mathrm{Tr}_A[FD(\xi_2)]\mathrm{Tr}_A[GD(\xi_1)], \tag{5}$$

where we have used the idenitiy $\mathrm{Tr}_A[D(\xi_1)G] = \mathrm{Tr}_A[GD(-\xi_1)]$ and $f(-\xi_1,\xi_2) = f(\xi_2,\xi_1)$ (see Appendix A of Ref. [34]). Through the above trace formula, we can express the second Rényi entropy for subsystem A, $S_A = -\ln \mathrm{Tr}_A\rho_A^2$ as

$$e^{-S_A^{(2)}} = \int d^2\xi f(\xi_1,\xi_2)\mathrm{Tr}_A[\rho_A D(\xi_1)]\mathrm{Tr}_A[\rho_A D(\xi_2)]. \tag{6}$$

Since, the displacement operator $D(\xi_\alpha)$ solely acts on subsystem A, we can write

$$\mathrm{Tr}_A[\rho_A D(\xi_\alpha)] = \mathrm{Tr}[\rho D(\xi_\alpha)], \tag{7}$$

where Tr denotes the trace over the entire system. Thus, to calculate subsystem Rényi entropy using Eq. (7), we do not need to explicitly deal with path integral representation of the reduced density matrix ρ_A. We only need to write down the path integral for $\mathrm{Tr}[\rho D(\xi_\alpha)]$, which only involves the trace of the total density matrix, albeit with the static auxiliary Grassmann source fields $\{\bar{\xi}_{i\in A,\alpha}, \xi_{i\in A,\alpha}\}$ inserted through the displacement operator $D(\xi_\alpha)$ in the path integral. These source fields only acts on the A subsystem. For example, if ρ is a thermal density matrix, $\rho \propto e^{-\mathcal{H}/T}$, for a system described by Hamiltonian $\mathcal{H}$ at temperature T ($k_B = 1$), then dynamical fermionic fields in the path integral follow the antiperiodic boundary condition, $c_i(\tau+\beta) = -c_i(\tau)$ in imaginary time τ, as in the usual thermal field theory [61]. Thus the path integral representation of subsystem Rényi entropy in Eq. (6) bypasses the use of more complicated boundary conditions in the standard path integral for entanglement [8]. We can also use the trace identity Eq. (5) recursively to express higher order Rényi entropy conveniently, as discussed in Refs. [34,35].

Notably, as n approaches 1, the Rényi entropy $S_A^{(n\to 1)}$ becomes the von Neumann entropy $S_A = -\mathrm{Tr}_A(\rho_A \ln \rho_A)$. However, as S_A involves the logarithm ($\ln \rho_A$) of the reduced density matrix, direct computation of von Neumann entropy is not possible within our path integral formalism or in the usual replica field theory method [8], or even in the determinantal QMC [20–27], which also uses the path integral representation. Hence, in the DMFT approximation for entanglement

developed here, we can only compute Rényi entropies. Moreover, we only focus on the second Rényi entropy which is easier to compute numerically compared to higher order Rényi entropies $S_A^{(n>2)}$.

III. THE PATH INTEGRAL FOR SUBSYSTEM RENYI ENTROPY FOR THERMAL STATE

In this section, we briefly discuss the path integral formalism [34] for subsystem Rényi entropy of fermions in a thermal state. For concreteness, we consider a system of spin-1/2 ($\sigma = \uparrow, \downarrow$) fermions on a lattice with N sites in thermal state at a temperature T described by a density matrix $\rho = e^{-\beta\mathcal{H}}/Z$ with Hamiltonian $\mathcal{H}$. Here $\beta = 1/T$ ($k_B = 1$) and Z is the partition function. In this work, we only consider the second Rényi entropy $S_A^{(2)}$ for simplicity. As discussed in the previous section, the path integral is constructed using Eqs. (6) and (7), and is given by

$$e^{-S_A^{(2)}} = \int d^2\xi\, f(\xi_1, \xi_2)\mathrm{Tr}[\rho D(\xi_1 \in A)]\mathrm{Tr}[\rho D(\xi_2 \in A)], \tag{8}$$

where "Tr" denotes trace over the entire system. The term $\mathrm{Tr}[\rho_A D(\xi)]$, called the characteristic function, can be written in terms of a coherent-state path integral [34],

$$e^{-S_A^{(2)}} = \frac{1}{Z^2}\int d^2\xi\, f(\xi_1, \xi_2)\mathcal{D}(\bar{c}, c)e^{-(\mathcal{S}+\mathcal{S}_\xi)}, \tag{9}$$

where $\mathcal{S} = \int_0^\beta [\sum_{i\sigma\alpha} \bar{c}_{i\sigma\alpha}(\tau)(\partial_\tau - \mu)c_{i\sigma\alpha}(\tau) + \mathcal{H}(\bar{c}, c)]$ is the *usual imaginary time action* for a Hamiltonian but with two replicas $\alpha = 1, 2$. The term $\mathcal{S}_\xi = \int_0^\beta \sum_{i\in A,\sigma}[\bar{c}_{i\sigma\alpha}(\tau)\delta(\tau - \tau_0^+)\xi_{i\sigma\alpha} - \bar{\xi}_{i\sigma\alpha}\delta(\tau - \tau_0)c_{i\sigma\alpha}(\tau)]$ acts like a source term which is nonzero on the A subsystem inserted at imaginary time τ_0 breaking both the periodicity of the imaginary time ($\tau \in [0, \beta)$) and space translational symmetry. We emphasize that the nontrivial part of the action S_ξ acting as a source term is not an *ad hoc* term added in the action but it originates *naturally* from the coherent state path integral representation of the displacement operator in Eq. (8) within the formalism of Rényi entropy, as discussed in Sec. II, and in our previous work [34]. The imaginary time τ_0 is arbitrary and can be placed anywhere on the thermal cycle $0 \leqslant \tau < \beta$. The fermionic fields have the usual antiperiodic boundary condition $c(\tau + \beta) = -c(\tau)$. For noninteracting systems, it is straightforward to integrate out [33–35] the fermionic fields $\bar{c}, c$ and the auxiliary fields $\bar{\xi}, \xi$ to obtain the Rényi entropy. As discussed in Ref. [34], for interacting systems treated within some nonperturbative approximations, like in large-N models, it is advantageous to first integrate out the Gaussian auxiliary fields in Eq. (8) and obtain

$$e^{-S_A^{(2)}} \equiv \frac{Z_A^{(2)}}{Z^2} = \frac{1}{Z^2}\int \mathcal{D}(\bar{c}, c)e^{-(\mathcal{S}+\mathcal{S}_{\mathrm{kick}})}, \tag{10}$$

where

$$\mathcal{S}_{\mathrm{kick}} = \sum_{i\in A,\alpha\beta\sigma} \bar{c}_{i\sigma\alpha}(\tau)M_{\alpha\beta}\delta(\tau - \tau_0^+)\delta(\tau' - \tau_0)c_{i\sigma\beta}(\tau'), \tag{11}$$

henceforth referred as the *kick* term which arises *naturally* within the formalism, corresponds to an effective time-dependent self-energy for the fermions at τ_0. The matrix

$$M = \begin{bmatrix} 1 & 1 \\ -1 & 1 \end{bmatrix} \tag{12}$$

couples the two replicas $\alpha = 1, 2$. In Ref. [34], we have used the path integral representation of Eq. (10) to evaluate $S_A^{(2)}$ of the SYK model and its several extensions. Below we show that the same representation can be utilized to formulate a DMFT for Rényi entanglement entropy in the Hubbard model.

A. Subsystem Rényi entropy via integration of the kick term

Using Eq. (10), the second Rényi entropy $S_A^{(2)}$ can be formally written as

$$S_A^{(2)} = \beta\big(\Omega_A^{(2)} - 2\Omega\big), \tag{13}$$

where we define $\Omega_A^{(2)} \equiv -T\ln Z_A^{(2)}$ and $\Omega = -T\ln Z$ is the thermodynamic grand potential. However, direct computation of both $\Omega_A^{(2)}$ and Ω for interacting systems is difficult in general and typically requires thermodynamic or coupling constant integration [34,62]. Here we find a new way to extract $S_A^{(2)}$ by using the kick term in Eq. (10). We consider the following quantity:

$$e^{-S_A^{(2)}(\lambda)} = \frac{Z_A^{(2)}(\lambda)}{Z^2} = \frac{1}{Z^2}\int \mathcal{D}(\bar{c}, c)e^{-(\mathcal{S}+\lambda\mathcal{S}_{\mathrm{kick}})}, \tag{14}$$

which reduces to $S_A^{(2)}(\lambda = 1) = S_A^{(2)}$, the second Rényi entropy, for $\lambda = 1$, and $S_A^{(2)}(\lambda = 0) = 0$. In the above, by taking the derivative with respect to λ, we get

$$\partial_\lambda S_A^{(2)}(\lambda) = \frac{\int \mathcal{D}(\bar{c}, c)e^{-(\mathcal{S}+\lambda\mathcal{S}_{\mathrm{kick}})}\mathcal{S}_{\mathrm{kick}}}{\int \mathcal{D}(\bar{c}, c)e^{-(\mathcal{S}+\lambda\mathcal{S}_{\mathrm{kick}})}} = \langle\mathcal{S}_{\mathrm{kick}}\rangle_{Z_A^{(2)}(\lambda)}, \tag{15}$$

i.e., the expectation value of the kick term with respect to the effective partition function $Z_A^{(2)}(\lambda)$. Integrating the above equation over λ from 0 to 1, we obtain an expression for the second Rényi entropy

$$S_A^{(2)} = \int_0^1 d\lambda\langle\mathcal{S}_{\mathrm{kick}}\rangle_{Z_A^{(2)}(\lambda)}. \tag{16}$$

The great advantage of the above expression is that the kick term is quadratic in Grassmann variables $\bar{c}, c$. In the above, we have assumed that no phase transition occurs as we vary λ. Such transition as a function of λ in the entanglement action might be present and will be interesting to study in the future. Assuming that there are no transitions with λ, the Rényi entropy can be obtained from Eq. (16) using

$$\langle\mathcal{S}_{\mathrm{kick}}\rangle_{Z_A^{(2)}(\lambda)} = \sum_{i\in A,\alpha\beta\sigma} M_{\alpha\beta}G_{i\sigma\beta,i\sigma\alpha}(\tau_0, \tau_0^+), \tag{17}$$

where the imaginary-time local single-particle Green's function

$$G_{i\sigma\alpha,i\sigma\beta}(\tau, \tau') = -\langle\mathcal{T}_\tau c_{i\sigma\alpha}(\tau)\bar{c}_{i\sigma\beta}(\tau')\rangle_{Z_A^{(2)}(\lambda)}. \tag{18}$$

The Green's function, however, needs to be evaluated in the presence of the kick term with variable λ. In the next section, we show how the Green's function can be obtained through the DMFT approximation.

IV. DYNAMICAL MEAN-FIELD THEORY FOR THE SECOND RÉNYI ENTROPY IN THE HUBBARD MODEL

We consider the nearest-neighbor Hubbard model

$$\mathcal{H} = \sum_{\langle ij\rangle,\sigma} t_{ij} c^\dagger_{i\sigma} c_{j\sigma} - \mu \sum_i n_i + U \sum_i n_{i\uparrow} n_{i\downarrow}, \tag{19}$$

where $t_{ij} = t$ is the nearest-neighbor hopping amplitude between lattice sites ($i = 1, \ldots, N$) on 1d and 2d square lattices, μ is the chemical potential, and U is the onsite repulsive interaction strength between fermions with opposite spins $\sigma = \uparrow, \downarrow$. Here, $n_{i\sigma} = c^\dagger_{i\sigma} c_{i\sigma}$ and $n_i = \sum_\sigma n_{i\sigma}$ are the electronic number operators. From here on, we set the hopping $t = 1$ as the unit of energy and temperature ($k_B = 1$). We write down the entanglement action $\mathcal{S}_\lambda = \mathcal{S} + \lambda S_{\rm kick}$ of Eq. (14) for the Hubbard model as

$$\mathcal{S}_\lambda = -\int_0^\beta d\tau d\tau' \sum_{ij,\sigma} \bar{c}_{i\sigma\alpha}(\tau) G^{-1}_{0,i\alpha,j\beta}(\tau,\tau') c_{j\sigma\beta}(\tau') + \int_0^\beta d\tau U \sum_{i\alpha} n_{i\uparrow\alpha}(\tau) n_{i\downarrow\alpha}(\tau), \tag{20}$$

where $G^{-1}_{0,i\alpha,j\beta}(\tau,\tau')$ is inverse noninteracting lattice Green's function in the presence of entanglement cut(s) between A and the rest of the systems, i.e.,

$$G^{-1}_{0,i\alpha,j\beta}(\tau,\tau') = -[(\partial_\tau - \mu)\delta_{ij} + t_{ij}]\delta(\tau-\tau')\delta_{\alpha,\beta} - \lambda\delta_{i\in A}\delta_{ij} M_{\alpha,\beta}\delta(\tau-\tau_0^+)\delta(\tau'-\tau_0). \tag{21}$$

As mentioned earlier in Sec. I, the self-energy kick, which only acts on A ($\delta_{i\in A} = 1$ for $i \in A$ and zero otherwise), breaks both lattice and time-translation symmetry in this formulation. As a result, we construct a single-site inhomogeneous nonequilibrium DMFT. We use the cavity method [40] to reduce the lattice problem into effective single-site problems for each of the sites $i = 1, \ldots, N$, described by the generating functions

$$Z^{(2)}_{\lambda,i} = \int \mathcal{D}(\bar{c}, c) e^{-\mathcal{S}_{\lambda,i}}, \tag{22}$$

where the effective action $\mathcal{S}_{\lambda,i}$ is given by

$$\mathcal{S}_{\lambda,i} = -\int_0^\beta d\tau d\tau' \sum_{\sigma\alpha\beta} \bar{c}_{\sigma\alpha}(\tau) \mathcal{G}^{-1}_{i,\alpha\beta}(\tau,\tau') c_{\sigma\beta}(\tau') + \int_0^\beta d\tau U \sum_\alpha n_{\uparrow\alpha}(\tau) n_{\downarrow\alpha}(\tau). \tag{23}$$

Here $\mathcal{G}_{i,\alpha\beta}(\tau,\tau')$ is the dynamical *Weiss* field, such that

$$\mathcal{G}^{-1}_i(\tau,\tau') = -(\partial_\tau - \mu)\delta(\tau-\tau')\mathcal{I} - \Delta_i(\tau,\tau') - \lambda\delta_{i\in A} M \delta(\tau-\tau_0^+)\delta(\tau'-\tau_0), \tag{24}$$

is a 2×2 matrix in the entanglement replica space, and $\mathcal{I}$ is the identity matrix in the same space. In the above, we have also assumed a paramagnetic state. Of course, like in equilibrium DMFT [40], the formulation can be easily extended, to describe entanglement in ordered states, such as the antiferromagnetic Néel state in the Hubbard model. The matrix $\Delta_i(\tau,\tau')$ in Eq. (24) is the hybridization function which can be expressed in terms of the lattice Green's function as discussed below. The impurity Green's function is related to the Wiess field via the Dyson equation,

$$G^{-1}_i(\tau,\tau') = \mathcal{G}^{-1}_i(\tau,\tau') - \Sigma_i(\tau,\tau'), \tag{25}$$

where $\Sigma_i(\tau,\tau')$ is the impurity self-energy. The Green's function can be obtained by solving the impurity problem using some approximate or exact impurity solvers [40,42], e.g., CTQMC [48]. In this work, for simplicity and as a first attempt to compute entanglement via DMFT within the new formalism [34], we use iterative perturbation theory (IPT) [40] to obtain the self-energy in Eq. (25).

We consider the particle-hole symmetric half-filling case with the chemical potential $\mu = U/2$. At half-filling, IPT, which retains the self-energy up to second order in U for the impurity problem, is known to work very well [40] in equilibrium, especially in the metallic phase. As well known, in this case, IPT coincides with the exact result for both $U \to 0$ and $U \to \infty$, i.e., the atomic limit, and thus it interpolates well between the two limits even at intermediate U. Here, it is also important to note that though IPT is a second-order skeleton approximation for the self-energy at the level of a single impurity, the self-consistent computation of the bath Green's function in DMFT through the lattice self-consistency, discussed below, adds an infinite number diagrammatic contributions to the self-energy with similar topology.

For the effective nonequilibrium problem [Eq. (22)], we also use the IPT as an approximate impurity solver. The IPT self-energy in our case is given by

$$\Sigma_{i,\alpha\beta}(\tau,\tau') = U G_{ii,\alpha\beta}(\tau,\tau^+)\delta(\tau'-\tau^+)\delta_{\alpha\beta} - U^2 \tilde{\mathcal{G}}^2_{i,\beta\alpha}(\tau,\tau')\tilde{\mathcal{G}}_{i,\alpha\beta}(\tau',\tau). \tag{26}$$

Here the first term is Hartree self-energy, and the second one is the second-order self-energy obtained using Hartree corrected Green's function

$$\tilde{\mathcal{G}}^{-1}_{i,\alpha\beta}(\tau,\tau') = \mathcal{G}^{-1}_{i,\alpha\beta}(\tau,\tau') - U G_{ii,\alpha\beta}(\tau,\tau^+)\delta(\tau'-\tau^+)\delta_{\alpha\beta}. \tag{27}$$

Within the single-site DMFT approximation, we assume the self-energy in the lattice problem to be local and the same as the impurity self-energy. Thus the lattice Green's function $G_{i\alpha,j\beta}(\tau,\tau')$ is obtained from the lattice Dyson equation

$$\int_0^\beta d\tau'' \sum_{k\gamma} \left[G^{-1}_{0,i\alpha,k\gamma}(\tau,\tau'') - \delta_{ik}\Sigma_{i,\alpha\gamma}(\tau,\tau'')\right] G_{k\gamma,j\beta}(\tau'',\tau') = \delta_{ij}\delta_{\alpha\beta}\delta(\tau-\tau'). \tag{28}$$

The DMFT loop is closed by relating the lattice Green's function with the hybridization function $\Delta_i(\tau,\tau')$. The latter can be obtained via the cavity method (see Appendix A 1 a) in terms of the cavity Green's function as

$$\Delta_{i,\alpha\beta}(\tau,\tau') = \sum_{jl} t_{ij} t_{il} G^{(i)}_{j\alpha,l\beta}(\tau,\tau'), \tag{29}$$

where the cavity Green's function, obtained with the ith site removed from the original lattice, is related to full lattice

Green's function via

$$G^{(i)}_{j\alpha,l\beta}(\tau,\tau') = G_{j\alpha,l\beta}(\tau,\tau') - \int d\tau_1 d\tau_2 \sum_{\gamma\delta} G_{j\alpha,i\gamma}(\tau,\tau_1) \times [G_{i\gamma,i\delta}(\tau_1,\tau_2)]^{-1} G_{i\delta,l\beta}(\tau_2,\tau'). \quad (30)$$

The above closes the DMFT self-consistency loop. For our numerical computations, we further make the large-connectivity Bethe lattice approximation [40] for the cavity Green's function. As a result, for the model [Eq. (19)] with only nearest-neighbor hopping, Eq. (29) becomes

$$\Delta_{i,\alpha\beta}(\tau,\tau') = t^2 \sum_j{}' G_{j\alpha,j\beta}(\tau,\tau'), \quad (31)$$

where $\sum_j'$ indicates that the summation is over only the nearest neighbors of i. This approximation makes the computation easier, keeping the essential features of the finite dimensionality through the lattice Green's function.

Computationally, the most expensive part of the DMFT loop here is the inversion of Eq. (28) to obtain the lattice Green's function $\mathbf{G}$, a matrix in indices $(i\alpha\tau, j\beta\tau')$. As discussed in the next section and in Appendix A, we discretize the imaginary time and use a recursive Green's function method for large systems to obtain $\mathbf{G}$. We also benchmark our results by doing direct inverse in Eq. (28) for small systems.

V. NUMERICAL SOLUTION OF DMFT EQUATIONS TO OBTAIN $S_A^{(2)}$

We solve the DMFT self-consistency Eqs. (24)–(29) and (31) by discretizing them in imaginary time τ with discretization step $\delta\tau$ as detailed in Appendix A. To evaluate $S_A^{(2)}$ from Eq. (16), we perform the DMFT calculation for λ ranging from 0 to 1 in steps of size $\delta\lambda$ as discussed in Appendix B. After obtaining the single-site self-consistent Green's function [Eq. (18)] for different λ, we use Eqs. (17) and (16) to compute $S_A^{(2)}(\delta\tau)$ for a given discretization $\delta\tau$. By repeating the calculation of $S_A^{(2)}(\delta\tau)$ for different $\delta\tau$ values and extrapolating to $\delta\tau \to 0$ limit, we finally obtain $S_A^{(2)}$. The details of the extrapolation process are discussed in Appendix D. As mentioned in the preceding section, we employ a recursive Green's function method to obtain the lattice Green's function from Eq. (28) (see Appendix A 1). By using the recursive Green's function method, we can compute $S_A^{(2)}$ for reasonably large systems, $N \leqslant 100$ in 1d, and $N \leqslant 20 \times 20$ in 2d up to low temperatures ($T \geqslant 0.05$, in units of nearest-neighbor hopping amplitude t). The results reported in the main text are for periodic boundary condition (PBC). We also discuss some results for open boundary condition (OBC) in Appendix F.

A. Comparison with the noninteracting limit and QMC

To benchmark the kick integration method of Eq. (16) and the extrapolation $S_A^{(2)}(\delta\tau \to 0)$, we first compare the results for $S_A^{(2)}$ for the noninteracting case ($U = 0$) with those calculated directly using the correlation matrix $C_{ij} = \mathrm{Tr}[\rho c_i^\dagger c_j]$ for $i, j \in A$. The latter calculation using C_{ij} can only be performed for noninteracting problems. The correlation matrix can be easily evaluated using the single-particle eigenenergies and eigenfunctions of the tight-binding model of Eq. (19) for $U = 0$. The second Rényi entropy is obtained from $S_A^{(2)} = -\mathrm{Tr}\ln[(1-C)^2 + C^2]$ [11,34]. As shown in Fig. 1, $S_A^{(2)}(\delta\tau \to 0)$ for different temperatures matches very well with the corresponding $S_A^{(2)}$ from correlation matrix calculation for a noninteracting system of size $N = 10$.

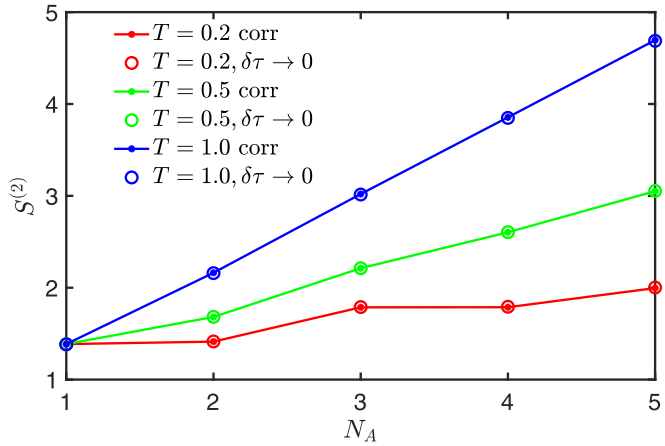

FIG. 1. The extrapolated $S_A^{(2)}(\delta\tau \to 0)$ (open circles) for $U = 0$ is compared with the $S_A^{(2)}$ from correlation matrix calculation (closed circle+line, "corr") for $N = 10$ and three different temperatures $T = 0.2,\ 0.5,$ and 1.0.

We next focus on the interacting problem and compare our DMFT results for $S_A^{(2)}$ with QMC data taken from Ref. [24] for $N = 32$ and $U = 2.0$. In Fig. 2, the $S_A^{(2)}$ as a function of subsystem size N_A for this two method is shown for high ($T = 1.0$) to intermediate temperatures ($T = 0.5, 0.2$). For high T, the results from our DMFT approach coincide with the QMC results. Even at intermediate temperatures, the comparison is reasonable given the fact that 1d is the worst-case scenario for a mean-field approach like single-site DMFT, and that too, employing an approximate impurity solver like IPT.

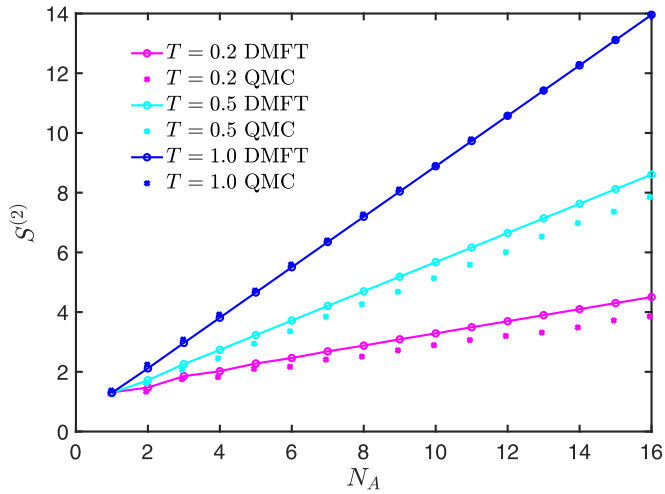

FIG. 2. DMFT results for $S_A^{(2)}$ as a function of subsystem size N_A in 1d Hubard model are compared with QMC data from Ref. [24] at three temperatures $T = 1.0,\ 0.5,$ and 0.2 for system size $N = 32$ and $U = 2$.

Nevertheless, it has been shown [46,47,63] that cluster extension of DMFT can capture some of the subtle Luttinger-liquid physics in 1d arising from long-distance correlations. Hence, cluster extensions of our DMFT approach will be able to provide in the future a good description of entanglement properties even in 1d.

Given the above benchmarks, in the next sections, we study the subsystem-size dependence and the entropy to entanglement crossover of $S_A^{(2)}$, first in 1d, and then for the 2d Hubbard model.

VI. $S_A^{(2)}$ IN 1D HUBBARD MODEL

In 1d, single-site DMFT gives rise to a metal-insulator transition at finite U [46,63] at half filling, unlike the exact Bethe ansatz solution [64]. The latter leads to a metallic state only at $U = 0$ and gapped states for any $U > 0$. The metallic state in DMFT is a relic of the infinite dimension inherent in the local self-energy approximation in single-site DMFT, even though some effects of finite dimension are fed back through the lattice self-consistency. We first look into $S_A^{(2)}(N_A, T)$ of this mean-field metallic state in 1d.

We note that, DMFT being an approximate theory, especially in its single-site implementation which is based on infinite dimensional approximation of local self-energy, is not expected to give accurate description of entanglement or any other properties of short-range 1d systems. However, since the entanglement DMFT formulated in Sec. IV is numerically much easier to implement in 1d than in higher dimensions, as a *proof of principle* and simpler demonstration of the implementation of our method we discuss here the DMFT results for entanglement in 1d half-filled Hubbard model. This also helps us to verify $U \to 0$ noninteracting result which can be obtained directly from correlation matrix approach. Despite the expected shortcomings of DMT in 1d, we find a very good agreement with QMC results in relatively higher temperature as discussed in the previous section.

In our DMFT formalism, the subsystem Rényi entropy is obtained from an imaginary-time path integral. Thus we perform the calculations at finite temperature with a finite discretization $\delta\tau$. To obtain the ground-state entanglement, we need to take the $T \to 0$ or $\beta \to \infty$ and $\delta\tau \to 0$ limit. This is not straightforward since at finite temperature $S_A^{(2)}$ contains both thermal and entanglement entropy contributions, and we need to *disentangle* these two contributions as the $T \to 0$ limit is taken. As discussed below, we find that the thermal to entanglement crossover in $S_A^{(2)}$ for the DMFT metallic state can be described by the crossover function known from CFT [8,12,19,49].

We show $S_A^{(2)}$ in Fig. 3 as a function of subsystem size N_A for 1d Hubbard model with periodic boundary condition. In Fig. 3(a), the result for $S_A^{(2)}$ vs. N_A is shown at low temperature $T = 0.05$ for the total system size $N = 50$ and interaction strengths $U = 0,\ 0.5,$ and 2. Figures 3(b) and 3(c) show $S_A^{(2)}(N_A)$ at relatively higher temperatures, $T = 0.1$ and 0.2, for $N = 100$ and $U = 0,\ 2,\ 3$. The $U = 0$ results are computed using the correlation matrix approach discussed in the preceding section, and $S_A^{(2)}$ for nonzero U is obtained through DMFT. At higher temperatures, $S_A^{(2)}$ for $N_A \gg 1$ is seen to vary linearly with N_A, i.e., a *volume law* scaling. This indicates

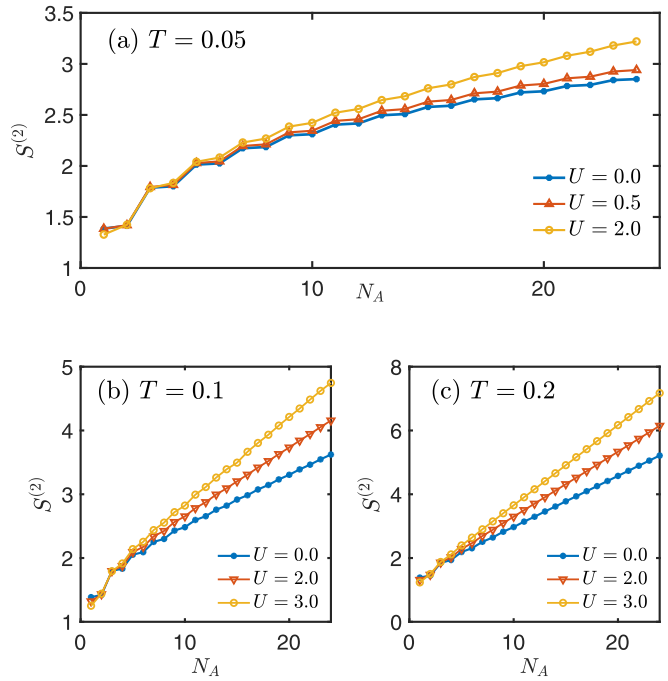

FIG. 3. Result for the second Rényi entropy $S_A^{(2)}$ in 1d Hubbard model with periodic boundary condition. (a) $S_A^{(2)}$ as a function of subsystem size N_A is shown for $U = 0, 0.5, 2$ and total system size $N = 50$ at temperature $T = 0.05$. $S_A^{(2)}(N_A)$ for $U = 0,\ 2,\ 3$ and $N = 100$ at (b) $T = 0.1$ and (c) 0.2. The $S_A^{(2)}$ for $U = 0.0$ are calculated using the correlation matrix and that for $U \neq 0$ using DMFT.

the dominance of thermal entropy at higher temperatures. An *arclike* feature emerges at lower temperatures. This is the hallmark of entanglement contribution to subsystem Rényi entropy. Thus the change of linear to arc-like behavior originates from entropy to entanglement crossover, as we discuss below.

Gapless 1d systems, such as critical bosonic or spin chains, and gapless fermionic chains, exhibit the logarithmic violation of the area-law scaling of entanglement. These systems are usually described by $1+1$ D CFT characterized by some central charge c [8,65]. The Rényi entropy $S_A^{(n)}$ at $T = 0$ for a thermodynamically large system ($N \to \infty$) with one gapless mode is given by the CFT formula for $N_A \gg 1$ [8,66,67]

$$S_A^{(n)} = \frac{1}{2}\left(1+\frac{1}{n}\right)\left(\frac{c}{6}\right)\ln(N_A) + b'. \tag{32}$$

The logarithmic term above is universal with the central charge c, and b' is a subleading nonuniversal constant originating from high-energy degrees of freedom. For finite N, and systems with periodic boundary condition [8], the above formula is modified to

$$S_A^{(n)} = \frac{1}{2}\left(1+\frac{1}{n}\right)\left(\frac{c}{6}\right)\ln\left[\frac{N}{\pi}\sin\left(\frac{\pi N_A}{N}\right)\right] + b'. \tag{33}$$

Similarly, one can obtain the Rényi entropy [8,12] at finite temperature and $N \to \infty$ as

$$S_A^{(n)} = \frac{1}{2}\left(1+\frac{1}{n}\right)\left(\frac{c}{6}\right)\ln\left[\frac{v\beta}{\pi}\sinh\left(\frac{\pi N_A}{v\beta}\right)\right] + b, \tag{34}$$

where v is a velocity and b is some nonuniversal constant. For noninteracting spinless fermions, $v = v_F$ is the Fermi velocity.

In this case, $S_A^{(n)}$ is obtained by adding the contributions of the two gapless chiral modes, i.e., the left (L) and right (R) movers, at the two Fermi points, each with the central charge $c_L = c_R = c = 1$. Eq. (34) reduces to Eq. (32) for $\beta \to \infty$, i.e., at zero temperature, to give us the ground-state Rényi entanglement entropies. For $\beta \to 0$, Eq. (34) reproduces thermal Rényi entropy, $S^{(n)} \simeq (1/2)(1 + 1/n)(\pi cT/6v)N_A$, e.g., the thermal entropy $S(T) = (\pi cT/6v)N_A$ ($n = 1$), scaling linearly with subsystem size. Therefore the expression Eq. (34) can be viewed as a crossover formula [18] from thermal to entanglement entropy. The same low-energy degrees of freedom give rise to the universal part of entanglement and thermal entropy and thus lead to the smooth crossover. The CFT formulas [Eqs. (32)–(34)] are also applicable for gapless states of interacting fermions in 1d, i.e., for a Luttinger liquid. In this case, the effect of interaction only enters in the crossover formula [Eq. (34)] through the renormalized Fermi velocity v, whereas the central charge remains unchanged.

As we discuss in the next section in more detail, for $d > 1$, the Fermi liquid state of interacting fermions at $T = 0$ also obeys the universal logarithmic scaling [15] of Eq. (32), which is independent of any Fermi liquid corrections or Landau parameters. The effect of interaction again only appears [15] in the thermal to entanglement crossover [Eq. (34)] through the renormalized v. The single-site DMFT [Sec. IV] with the IPT approximation [41] is designed to give rise to a Fermi liquid metallic state even in 1d. Thus we describe our DMFT findings for $S_A^{(2)}(N_A, T)$ in the paramagnetic metallic state of the 1d Hubbard model, using the CFT expression outlined in Eq. (34), with the constant c replaced by $4c$. This substitution accounts for the two chiral modes from two Fermi points and two spin channels for each mode. We note that in more accurate treatment of 1d Hubbard model at half filling with finite $U > 0$, the charge modes will be gapped [64]. Hence, one expects logarithmic scaling of the entanglement only from the gapless spin modes and the replacement of c in Eq. (34) by $2c$ instead of $4c$. However, as already mentioned, such 1d physics of spin-carge separation and the gapping of the charge degrees of freedom is not captured by the DMFT. We note that Eq. (34) is valid for thermodynamically large systems ($N \to \infty$). For finite N and T, the analytical expression for $S_A^{(n)}(N_A, T, N)$ is not known [8,49,68] to the best of our knowledge. Nevertheless, we use Eq. (34) to describe our DMFT data for relatively large systems like $N = 50$ and 100, as shown in Fig. 3, and assuming N to be large enough so that finite N corrections may be neglected. Alternatively, we can consider the crossover function [Eq. (34)] as a fitting function, using which we can in principle fit $S_A^{(2)}$ as a function of N_A for a fixed T and the fitting parameters c, v and b (Appendix E). However, to reduce the number of fitting parameters, we independently extract the ratio (c/v) by fitting the low-temperature specific heat (per site) c_V from equilibrium DMFT calculations [see Appendix E 1] with the CFT expression $c_V = (\pi T/3)(c/v)$.

With the (c/v) ratio determined, we fit Eq. (34) to our data with two parameters c and b. As shown in Fig. 4(a), $S_A^{(2)}$ follows the crossover function quite well. The extracted central charge c is shown as a function T for fixed U, and as a function of U for a fixed T in Figs. 4(b) and 4(c), respectively. The nonuniversal fitting parameter b and the extracted normalized Fermi velocity v are shown in Appendix E 1. We find that

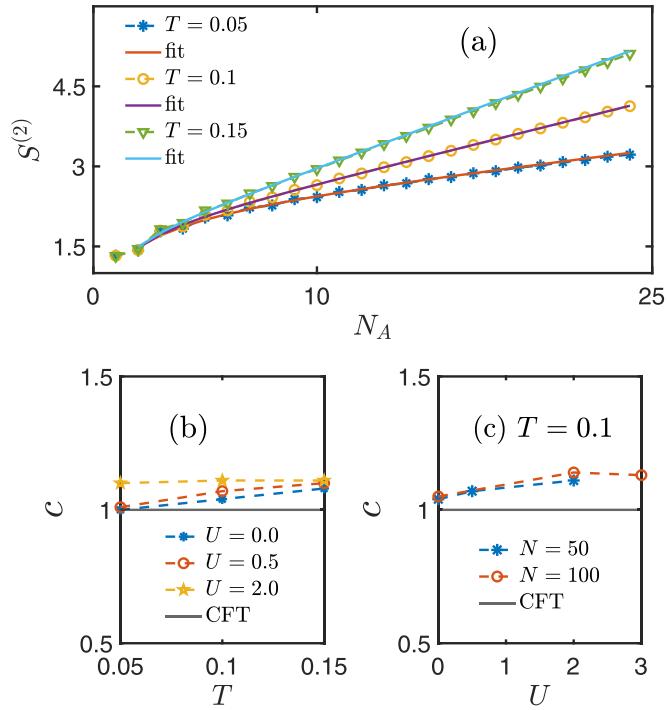

FIG. 4. (a) The second Rényi entropy $S_A^{(2)}$ (dashed line + marker) as a function subsystem size N_A for interaction strength $U = 2.0$ and system size $N = 50$ at $T = 0.05$, 0.1, and 0.15 is shown with the fitted CFT crossover function (line) of Eq. (34). (b) The extracted central charge c as a function of T is shown for different interaction strengths $U = 0$, 0.5, 2, and compared with the CFT value $c = 1$ (solid line). (c) The central charge c as a function of U is shown at $T = 0.1$ for two system sizes.

the extracted central charge is close to the free-fermion value $c = 1$. With decreasing temperature, the extracted central charge approaches $c = 1$ for the noninteracting ($U = 0$) and weakly interacting ($U = 0.5$) systems [Fig. 4(b)], and seems to deviate slightly for relatively stronger interaction $U = 2$. However, the deviation might be an artifact of employing the $N \to \infty$ formula [Eq. (34)] for finite N. In Fig. 4(c), we see that $N = 50$ and $N = 100$ give very similar values of $c \simeq 1$ at $T = 0.1$ as a function of U, thus assuring convergence at least for the range of N accessed in our calculations. In summary, we conclude that the entanglement properties of the DMFT Fermi liquid, captured through $S_A^{(2)}(N_A, T)$, and accessed within the local self-energy approximation match quite well with that of CFT.

VII. $S_A^{(2)}$ IN 2D HUBBARD MODEL

In this section, we discuss the results for $S_A^{(2)}$ in 2d Hubbard model for metallic (Fermi liquid) and Mott phases. The DMFT approximation typically provides a good description for equilibrium and nonequilibrium properties of strongly correlated systems in three dimension, while it falls short as an accurate description in two dimensional systems. However, DMFT has been applied for 2d systems to capture correlated phenomena in many previous works [56–59]. Moreover, Walsh *et al.* [53] employed the equilibrium cluster DMFT approximation to compute single-site Rényi entanglement

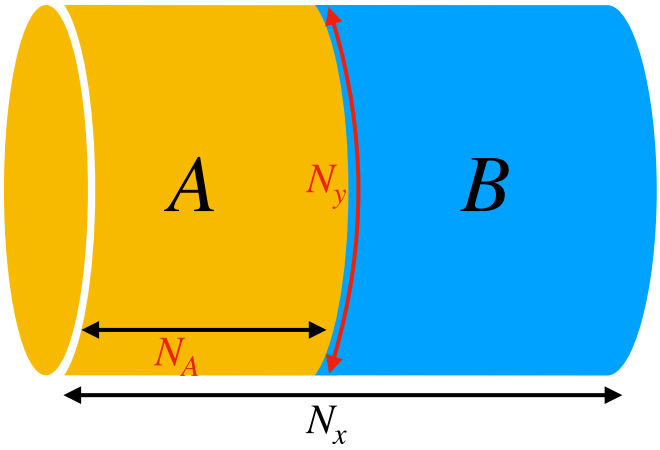

FIG. 5. The cylindrical subsytem A, with N_A sites in x direction and N_y sites in the y direction, used for computing entanglement in 2d Hubbard model, is shown. The periodic boundary condition is applied to the whole system in both x and y directions.

entropy in 2d Hubbard model. Therefore our DMFT based entanglement computation serves as a first approximation to compute entanglement in correlated systems in 2d. Our formalism of computing entanglement using the "kick" term, naturally allows us to develop the DMFT framework, presented in this paper, for accessing multi-site entanglement instead of being limited to a single site. Thus our endeavour could serve as a first step to explore more sophisticated approximations, such as extending the approach to cluster DMFT [56].

We consider the system with periodic boundary conditions in both x and y directions, i.e., a torus geometry for the system. We subdivide the system along the x axis, meaning, the entanglement cut is parallel to the y axis like in a cylindrical subsystem geometry as shown in Fig. 5. Due to the entanglement cut, the translational symmetry in the x-direction is broken while retaining the translation symmetry in the y direction, along which periodic boundary condition is applied. As discussed in Appendix G, the periodic boundary condition along the y axis allows the wave vector k_y to be a good quantum number, and makes the inversion of the lattice Green's function of Eq. (28) easier. In this case, Eq. (28) can be decoupled for each k_y mode. We discuss below our results for $S_A^{(2)}$ and its dependence on the subsystem size N_A, temperature, and interaction strength.

Most systems in higher dimension ($d > 1$) follow boundary law scaling of entanglement. Even the higher dimensional CFT gives strict boundary law scaling. However, there are several important exceptions [15–18] with logarithmic violation of the boundary law, e.g., free fermions, Fermi liquids, Weyl fermions in a magnetic field, non-Fermi liquids with critical Fermi surface, and Bose metals. Here we focus on Fermi liquid metallic state as captured within DMFT. The underlying reason behind the violation of the area law is that these systems with Fermi surface can be effectively described as a collection of patches on the Fermi surface [15,50]. Each of these Fermi surface patches acts as a one-dimensional gapless chiral mode described by $1+1$ D CFT. These modes are chiral as they can only propagate with Fermi velocity radially outward to Fermi surface at very low temperatures. Then, the scaling of entanglement entropy with N_A is simply the one-dimensional logarithmic scaling multiplied by the number of gapless $1+1$ D CFT modes [15]. The counting of the number of these mode depends on both the geometry of the Fermi surface and real space boundary [15].

As discussed in the preceding section, for one dimension, we have both right and left movers mode with central charge $c_L = c_R = c = 1$ and the scaling of Rényi entanglement entropy is given by Eq. (32). For the chiral mode in $d > 1$, we have either $c_L = 0,\ c_R = c$ or $c_R = 0,\ c_L = c$, and hence the contribution (per spin component) of each chiral mode to the Rényi entropy at $T = 0$ is still given by Eq. (32). The counting of the mode is obtained from the Widom formula [13,15–17,69,70], originally developed in the context of signal processing [71],

$$N_{\text{modes}} = \frac{1}{(2\pi)^{d-1}} \frac{1}{2} \int_{\partial A_x} \int_{\partial A_k} dA_x dA_k |\hat{\boldsymbol{n}}_x \cdot \hat{\boldsymbol{n}}_k|. \tag{35}$$

The integrals are over the real-space boundary ∂A_x of the subsystem and the Fermi surface ∂A_k. $\hat{\boldsymbol{n}}_x$ and $\hat{\boldsymbol{n}}_k$ are the unit normals to the real-space boundary and the Fermi surface, respectively. Here, the *flux factor* $|\hat{\boldsymbol{n}}_x \cdot \hat{\boldsymbol{n}}_k|$ counts the fraction of modes perpendicular to real-space boundary coming from a Fermi surface patch at $\boldsymbol{k}$. The Widom formula has been verified numerically [14] for free fermions in $d > 1$. For Fermi liquids, where only forward scattering is relevant, the Widom formula is expected to remain valid [15,50] with the same c in Eq. (32) modulo possible modification of the Fermi surface geometry due to interactions if any. Going beyond Fermi liquids, the Widom formula may get violated [72,73] or modified [18], e.g., as in the case of gapless states of composite fermions in the fractional quantum Hall regime, quantum spin liquids, and non-Fermi liquids.

For the square lattice Hubbard model [Eq. (19)] that we consider here, the noninteracting dispersion is $\varepsilon_k = -2t(\cos k_x + \cos k_y)$. Thus we can compute the N_{modes} for the cylindrical subsystem ($N_A \times N_y$) as discussed in Appendix H. In this case, N_{modes} is given by $2N_y$, where N_y is the number of sites in the y direction along the entanglement cut. Therefore, taking the spin degeneracy into account, we expect

$$S_A^{(2)}/N_y = \frac{c}{2} \ln(N_A) + b' \tag{36}$$

at $T = 0$. Moreover, like in the 1d case [Eq. (34)], we expect entropy to entanglement crossover at finite temperature for a thermodynamically large system to be given by

$$S_A^{(2)}/N_y = \frac{c}{2} \ln\left[\frac{v\beta}{\pi} \sinh\left(\frac{\pi N_A}{v\beta}\right)\right] + b, \tag{37}$$

where b is again another nonuniversal constant. Hence, the Rényi entropy per unit length along y direction, i.e., $S_A^{(2)}/N_y$ in this cylindrical subsystem geometry has a similar form as the 1d crossover formula in Eq. (34). Likewise, as in the 1d case, we do not have any crossover formula that interpolates between entanglement and thermal entropy for finite N and finite temperature. For the correlated metallic state obtained in our DMFT calculations for the 2d Hubbard model, we verify the crossover formula [Eq. (37)]. Again the effect of interactions only enters in the crossover formula via the velocity v for a

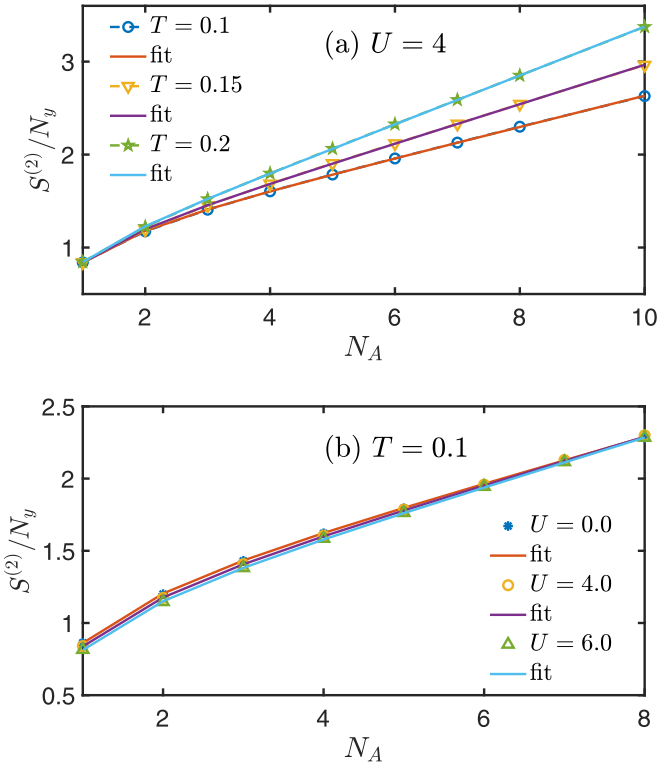

FIG. 6. (a) $S_A^{(2)}/N_y$ for the metallic state of 2d Hubbard model is shown for a $N = 20 \times 20$ lattice as a function of the subsystem length along x-axis N_A for temperatures $T = 0.1,\ 0.15,$ and 0.2 at fixed interaction strength $U = 4$. The results (dashed line+marker) fit well with the crossover function (line) of Eq. (37). (b) $S_A^{(2)}/N_y$ (filled circle, open circle, triangle) as a function of N_A is shown for different interaction strengths $U = 0,\ 4,$ and 6 at fixed $T = 0.1$. The corresponding fits (line) to the crossover function are also shown.

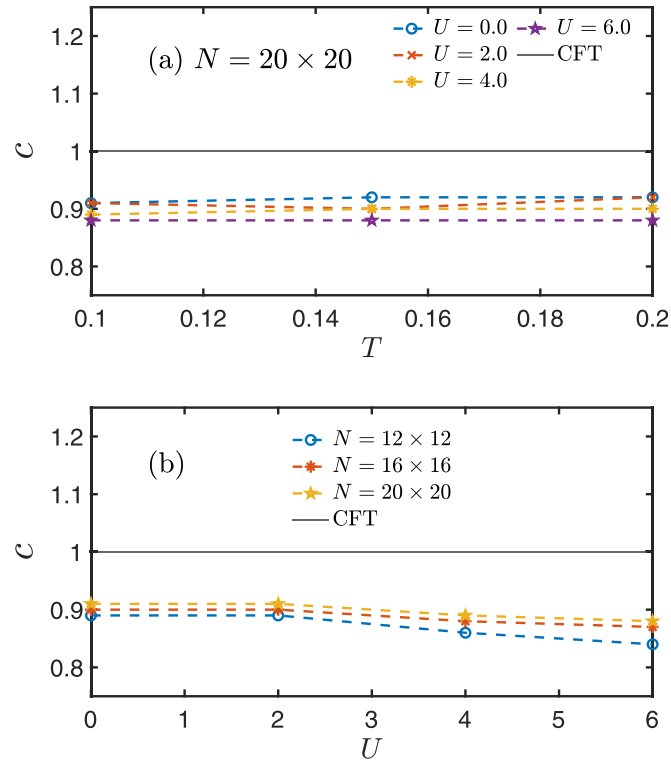

FIG. 7. (a) The extracted central charge c as a function of T is shown for different interactions $U = 0, 2, 4, 6$ and system size $N = 20 \times 20$, and compared with the CFT value $c = 1$. (b) The variation of the c as a function of U is shown at fixed $T = 0.1$ for different system sizes N, as indicated in the legends.

Fermi liquid. We note that a universal entropy-entanglement crossover formula may be valid more generally, even beyond Fermi liquids. Similar crossover formulas, constrained by the temperature dependence of thermal entropy, have been proposed [18] to hold even for gapless fermionic systems not described by Fermi liquid theory or devoid of quasiparticles, e.g., non-Fermi liquids with critical Fermi surfaces.

We compute the second Rényi entropy $S_A^{(2)}$ as a function of subsystem size $N_A N_y$ for a total system size $N_x N_y$. Here N_A is the number of lattice sites in the subsystem A in the x direction, and N_x and N_y are the total number of sites in the x and y directions, respectively. We vary the subsystem size by varying N_A while keeping N_y fixed. In Fig. 6(a), $S_A^{(2)}/N_y$, computed from DMFT, is shown as a function of N_A at low temperatures, $T = 0.1,\ 0.15,$ and 0.2, for $U = 4$ and system size $N = 20 \times 20$. We find that the crossover formula in Eq. (37) fits very well with our result as demonstrated in Fig. 6(a). Similarly, in Fig. 6(b), the $S_A^{(2)}/N_y$ is shown for different interaction strengths $U = 0,\ 4,$ and 6 at fixed $T = 0.1$ with the corresponding fits to the crossover formula [Eq. (37)] for a 20×20 system.

The c extracted from the above fittings is shown in Fig. 7. More details are given in Appendix H. Figure 7(a) shows the extracted c as a function of T for $U = 0,\ 2,\ 4,\ 6,$ and compares with the expected CFT value $c = 1$. We see that the calculated $c \simeq 0.9 < 1$, and c does not vary much with T. We find that $c \simeq 0.9 < 1$ even for $U = 0$, i.e., c deviates from 1 by more or less the same amount even for the noninteracting case for the system sizes studied. Thus, presumably, the deviation from the CFT value stems from the application of the crossover formula [Eq. (37)] for the thermodynamic limit to the finite systems. In Fig. 7(b), where we plot c as a function of U for different N values and $T = 0.1$, we observe that c decreases slightly for larger U and tends to increase very slowly with increasing N for a given U, implying that c might approach the expected value of 1 for larger systems. However, in the absence of an analytical crossover function for finite N and T, and for the accessible system sizes in our calculations, it is hard to extrapolate c to the $N \to \infty$. Nevertheless, we can conclude that modulo finite-size effects, our DMFT results for $S_A^{(2)}(N_A, T, N)$ for the metallic state of the 2d Hubbard model at half filling are consistent with the Widom formula and the expected logarithmic violation of area law for Fermi liquids [15].

We also compute the Rényi entropy deep inside the insulating phase at low temperature, as shown in Fig. 8 for $U = 14$. We find that $S_A^{(2)}/N_y$ is linear in N_A with a slope $\gtrsim \ln 2$, with a very weak dependence on T. This is expected due to the spin degeneracy of the paramagnetic Mott insulating state described by the DMFT for subsystem Rényi entropy implemented in this work. For the thermal grand canonical density matrix accessed in our DMFT, the thermal entropy (per site),

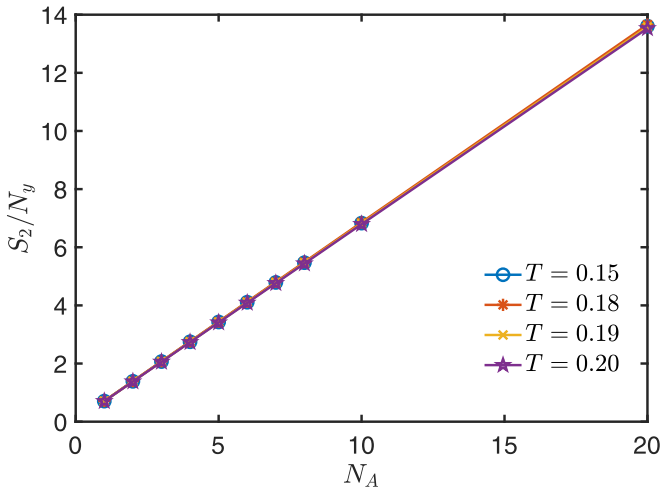

FIG. 8. The $S_A^{(2)}/N_y$ as a function of N_A is shown for several T's at fixed $U = 14$. This is computed from system size 20×20.

and thus the subsystem Rényi entropy $S_A^{(2)}/N_A$, approaches its maximal value, $S/N = \ln 4$, at very high temperatures, $T \gg U,\ W$, where W is noninteracting bandwidth. We note that though the limit $T \gg U,\ W$ is not feasible in any realistic material, this limit serves as a valuable theoretical limit to verify the validity of our formalism for extracting entanglement within the DMFT framework. Even at $T \to 0$, the paramagnetic Mott insulating state, unlike the Fermi liquid metallic state, retains the spin degeneracy of 2^N. This degeneracy leads to a residual zero-temperature entropy $S/N = \ln 2$, which is captured by the paramagnetic Mott insulating solution in the single-site DMFT as discussed in Ref. [40]. This residual entropy also contributes to the subsystem Rényi entropy in our path integral or DMFT formulation for the thermal mixed state. As a result, the subsystem Rényi entropy computed in this work does not approach true ground-state entanglement for the paramagnetic Mott insulating phase. Our formulation for entanglement path integral can be extended to describe pure states where true entanglement can be extracted even for the paramagnetic Mott insulator. This will be addressed in future works [74].

However, the paramagnetic state is not expected to be a true ground state in the Mott insulating phase, certainly not for unfrustrated lattices like square lattice [40]. Any magnetic order, like the antiferromagnetic Néel order expected in the Mott insulating phase of half-filled Hubbard model will quench the residual entropy to zero as $T \to 0$. As in the equilibrium single-site DMFT formulation [40], our entanglement DMFT can be readily extended to incorporate antiferromagnetic order at the mean-field level, as we discuss in Appendix I.

VIII. MUTUAL INFORMATION ACROSS MOTT TRANSITION IN 2D HUBBARD MODEL

Here we discuss the second Rényi mutual information as an entanglement and information-theoretic measure at finite temperature in the temperature versus interaction (T-U) phase diagram of the Hubbard model. The second Rényi mutual information [51,75]

$$I(A,B) = S_A^{(2)} + S_B^{(2)} - S_{A\cup B}^{(2)} = -\left(\ln Z_A^{(2)} + \ln Z_B^{(2)} - \ln Z_{A\cup B}^{(2)} + 2\ln Z\right) \quad (38)$$

is obtained from the combination of the Rényi entropies of a subsystem A, its complement B, and the whole system $A \cup B$. While the entanglement entropy can characterize pure states, e.g., ground state and quantum phase transitions between ground states at $T = 0$, the mutual information is a better information-theoretic measure for finite-temperature phases and phase transitions [76–79]. The mutual information is dominated by entanglement contribution when classical correlations are short-ranged, e.g., at low temperatures away from a finite-temperature critical point [51]. Moreover, different parts of mutual information can exhibit critical properties [76–79] at temperatures related to the finite-temperature critical point, e.g., at critical temperature T_c, and at $2T_c$ due to critical behaviors of $Z_A^{(2)},\ Z_B^{(2)}$ in Eq. (38) from the edges and corners of the subsystem $A,\ B$.

For a pure-state density matrix, $I(A,B) = 2S_A^{(2)}$. The $S_A^{(2)}$ for thermal density matrix at finite temperature contains both entanglement and thermal entropy contributions. However the (Rényi) mutual information, by construction, naturally excludes the volume-law thermal entropy of the subsystem and its complement. Thus mutual information follows in general an area-law scaling with subsystem size and captures both quantum (entanglement) and classical correlations between the subsystems. The study of Mott transition through the lens of mutual information is less explored in literature. In Refs. [53–55], the authors have studied the Mott transition in the 2d Hubbard model using equilibrium CDMFT through the mutual information of a *single* site and the rest of the system. They detect first-order phase transitions and the supercritical regime for $T > T_c$. The calculation of the single-site mutual information only requires the knowledge of occupation and double occupancy, which can be computed within equilibrium DMFT. The subsystem size scaling of mutual information cannot be captured within such equilibrium DMFT. Within our new path integral approach, we can easily study the subsystem size scaling of mutual information across Mott transition, as we discuss below.

To characterize the metal, insulator, and the phase transition separating these states at finite temperature, we first briefly discuss the T-U phase diagram of the half-filled 2d Hubbard model within large connectivity Bethe lattice approximation in DMFT [40]. We draw the T-U phase diagram by monitoring the equal time correlation function $D = \langle n_\uparrow n_\downarrow \rangle$ corresponding to the double occupancy of a site within equilibrium DMFT (Appendix E 1) as a function of U for different temperatures. A representative plot for double occupancy D versus U at $T = 0.14$ is shown in Fig. 9(a). The hysteresis behavior is due to the coexistence of both metal and insulator solution across the first-order Mott metal-to-insulator transition. The area of the hysteresis loop shrinks to zero as the first order transition ends at finite temperature Mott critical point (U_c, T_c). By monitoring $D(U)$, we obtain the T-U phase diagram, as shown in Fig. 9(b). The critical point is at $(U_c, T_c) \approx (9.9, 0.18)$.

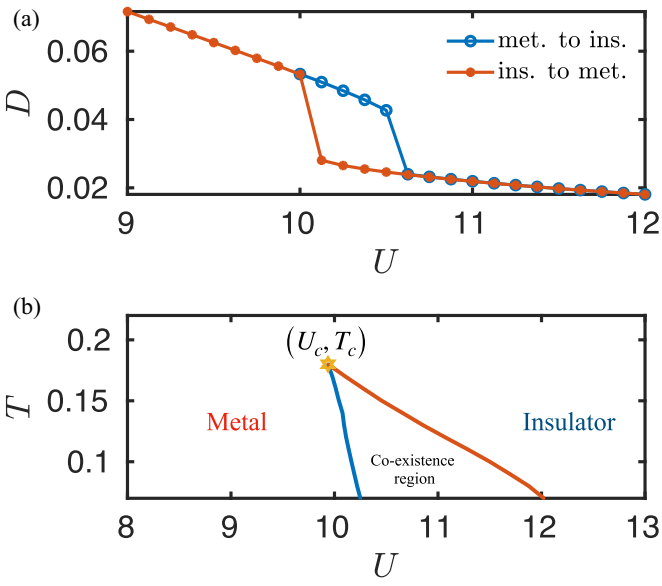

FIG. 9. (a) Double occupancy D, computed within single-site DMFT, as a function of U is shown at $T = 0.14$ for 2d Hubbard model. The legend "met. to ins." implies increasing U from the metal to insulator and "ins. to met." decreasing U the other way round. (b) The phase diagram for 2d half-filled Hubbard model constructed based on the double occupancy D is shown. (U_c, T_c) represents Mott critical point where the first-order line, or the coexistence region, ends. In the coexistence region, both metal and insulator solutions exist.

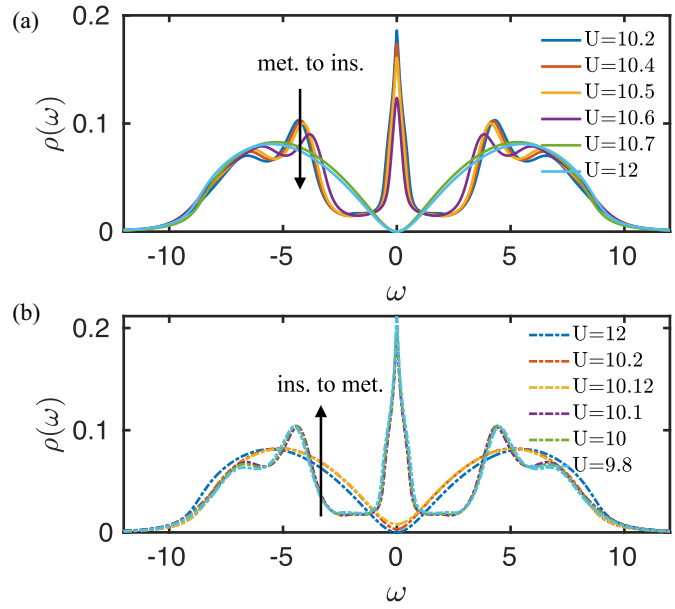

FIG. 10. Equilibrium spectral function $\rho(\omega) = -(1/\pi)\mathrm{Im}G_R(\omega)$ vs frequency (energy) ω is shown here for $T = 0.14$ for different U's: (a) $\rho(\omega)$ is calculated as a function of the increasing value of U starting from metallic state, i.e., for metal to insulator (met. to ins.) sweep. (b) $\rho(\omega)$ is calculated with decreasing U starting from an insulator state, i.e., an insulator to metal sweep. The $\rho(\omega \to 0) \neq 0$ characterizes metallic state at finite T.

The evolution of the one-particle spectral function, $\rho(\omega) = -(1/\pi)G_R(\omega)$, where $G_R(\omega)$ is the real-frequency retarded equilibrium Green's function, near coexistence region also demonstrates the first-order metal-insulator transition, consistent with double occupancy $D(U)$ from the imaginary-time equilibrium DMFT calculation (Appendix E 1). The one-particle spectral function changes its character from metallic to insulating at different values of U for a fixed T or different T for fixed U, depending on the sweep either from metal to insulator or insulator to metal. These are illustrated in Fig. 10 for different values of U at $T = 0.14$, and for various T values at a fixed $U = 10.1 \gtrsim U_c$ in Fig. 11, depicting the transition from metal to insulator or vice versa. Therefore we demonstrate the first-order Mott metal-insulator transition in equilibrium for the square-lattice Hubbard model through both double occupancy $D(U)$ and one-particle spectral function. It is worth *emphasizing* that the computation of the subsystem Rényi entropy relies on completely independent inhomogeneous DMFT calculations in the presence of a "kick" term, causing the Green's function $G(\tau, \tau')$ to depend on two time arguments (τ, τ'). Therefore the results from the equilibrium DMFT calculations, such as the spectral function shown in Figs. 10 and 11, does not enter in any way in our numerical computation of subsystem Rényi entropy through the new entanglement DMFT method.

In Fig. 12, the mutual information per site $I(A, B)/N_y$ along the y direction for the equal bi-partition $N_A = N_B$ is shown for $T = 0.16 < T_c$ and system size $N = 16 \times 16$. As mentioned earlier, for the first-order Mott transitions, two co-existing

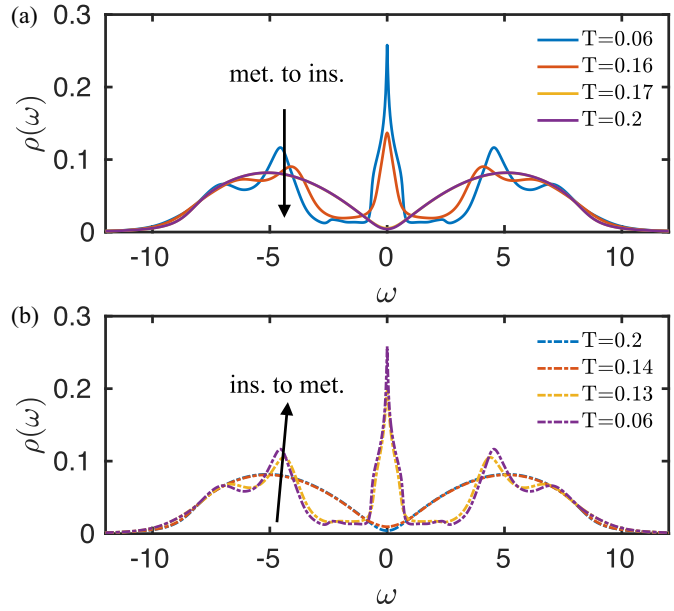

FIG. 11. Equilibrium spectral function $\rho(\omega) = -(1/\pi)\mathrm{Im}G_R(\omega)$ vs frequency (energy) ω is shown for $U = 10.1$ for different T's: (a) $\rho(\omega)$ is calculated as a function of the increasing value of T starting from the metallic state ($T = 0.06$) to insulator state ($T = 0.2 > T_c$), i.e., for metal to insulator (met. to ins.) sweep. (b) $\rho(\omega)$ is calculated with decreasing T starting from an insulator state ($T = 0.2$) to reach metallic state at $T = 0.06$, i.e., an insulator to metal sweep. Notice that insulator-to-metal transitions happen at different values of T than metal-to-insulator in (a). The $\rho(\omega \to 0) \neq 0$ characterizes metallic state at finite T.

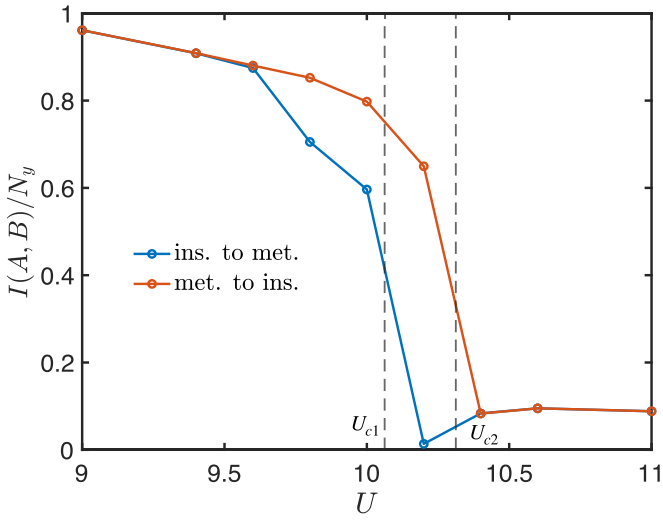

FIG. 12. The bipartite mutual information for $N_A = N_B$ per site of the subsystem along y axis, i.e., $I(A,B)/N_y$ as a function of interaction U at $T = 0.16 < T_c$ is shown for a $N = 16 \times 16$ lattice. "Met. to ins" refers to sweeping U from the metal to insulator phase and "ins. to met" for the other way round.

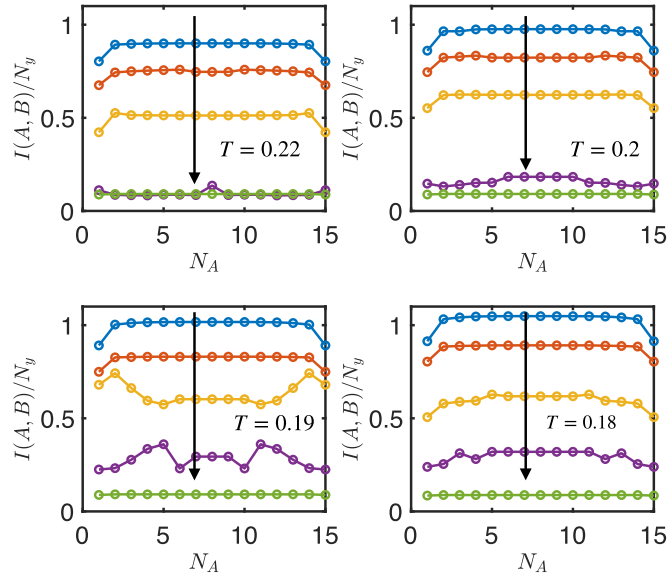

FIG. 13. The mutual information $I(A,B)/N_y$ for $N = 16 \times 16$ as a function of the length of subsystem N_A along x direction is shown here across the Mott metal-insulator transition for different interaction strength U ($U = 8.0, 9.0, 9.6, 10.0, 11.0$) and temperatures. U gradually increases from top to bottom, as indicated by the arrow, in each plot for a fixed temperature.

solutions, metal, and insulator, appear in the phase diagram as indicated in Fig. 9(b). In equilibrium DMFT, for $T < T_c$, starting from the insulating solution at large U and on decreasing the interaction slowly, a sudden jump to the metallic solution occurs at $U_{c1}(T)$, i.e., at the limit of metastability of the insulating phase, which is consistent with a first-order transition. Similarly, sweeping U from the metallic side leads to a jump to the insulating solution at $U_{c2}(T)$. For $T = 0.16$, U_{c1} and U_{c2} computed from double occupancy within the equilibrium calculation are shown in Fig. 12 as dotted vertical lines. The DMFT for Rényi entropy also leads to similar hysteresis behavior in the mutual information, as shown in Fig. 12, where the calculation of $I(A,B)$ vs. U is done in steps of $\delta U = 0.2$. Following the behavior of double occupancy, the bipartite mutual information $I(A,B)/N_y$ also jumps across U_{c1}, U_{c2}. Thus the mutual information between two extended subsystems can detect the first order nature of phase transitions, like the single-site mutual information [53–55]. Finite but weak correlations, indicated by the nonzero mutual information, persist even in the insulating phase for $U \gtrsim U_{c2}$, as can be seen in Fig. 12. We expect these correlations to approach zero for large interaction strengths $U \gg W$, where W is the noninteracting bandwidth.

The calculation of mutual information near the critical point (U_c, T_c) through the extrapolation $\delta\tau \to 0$ becomes challenging due to multiple solutions as well as very close numerical values of $S^{(2)}(\delta\tau)$ for different $\delta\tau$'s. For this reason, we present the data for a fixed $\delta\tau = 0.029$, without any extrapolation, in this section.

The subsystem size scaling of mutual information is expected to be of the form [76,77] $I(A,B) = I(N_A, N_y, \beta) \simeq a(\beta, N_A)N_y + d(\beta, N_A) + \mathcal{O}(N_y^{-1})$, with coefficients a and b weakly dependent on N_A. In our subsystem geometry, the dominant contribution to $I(A,B)$ comes from the interface of the two subsystems A and B, and leads to the leading area law ($\propto N_y$) for the mutual information with the coefficient $a(N_A, \beta)$. The latter is expected to approach a constant value with subsystem size N_A for sufficiently large N_A. The other term $d(N_A, \beta)$ can appear due to the corner contribution or, for a finite system, from the degeneracy of thermodynamic state, arising from symmetry breaking [76,77] or configurational entropy. In our subsystem geometry (Fig. 5), the corner contribution is absent. The finite-temperature Mott transition is similar to a liquid-gas transition [80]. Thus, for the second Rényi mutual information, constant term $d(\beta, N_A)$ can appear between $T_c < T < 2T_c$ and $T < T_c$ from effective Ising-like symmetry breaking in different parts of $I(A,B)$ along the first-order transition line in the T-U plane. We show $I(A,B)/N_y$ for $N = 16 \times 16$ lattice as a function of N_A in Fig. 13 for different Us across Mott transition at several temperatures near Mott critical point. The arrows in the plots indicate increasing values of interaction over the range $U = 8 - 11$. In Fig. 13, we see that $I(A,B)/N_y$ becomes more or less independent of N_A for $N_A \sim N/2$, except near the critical point (U_c, T_c), where more complex dependence on N_A is seen.

Finally, in the Fig. 14, we show the mutual information $I(A,B)/N_y$ for the bipartition $N_A = N_B$ as a function of temperature (in logarithmic scale) near $U \simeq U_c = 10.0$. The $I(A,B)$ shows a nonmonotonic behavior with T. In particular, the mutual information appears to dip between $\sim T_c$ and $\sim 2T_c$. A substantial $I(A,B)$, indicating correlations, persists even far above T_c till $T \lesssim W$ in the supercritical regime [53–55]. In the future, it will be interesting to study the system-size scaling of $I(A,B)$ with N_y or N to understand the nature of correlations in the supercritical regime contributing to the mutual information of an extended subsystem.

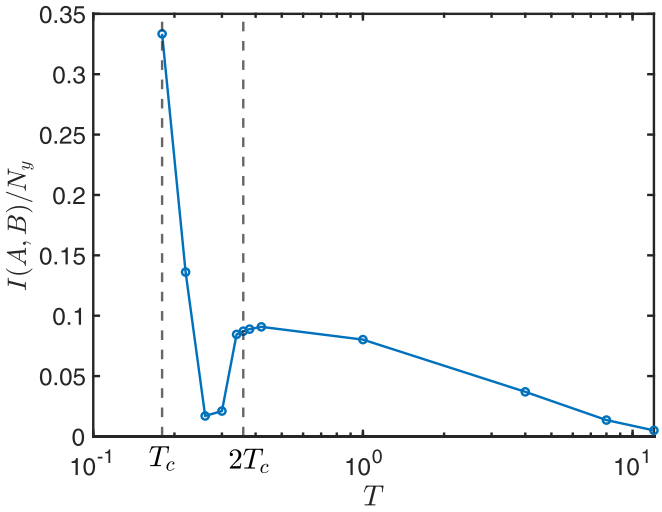

FIG. 14. The nonmonotonic temperature dependence of $I(A, B)/N_y$ is shown for $U = 10.0 \approx U_c$. This is computed from system size 16×16. Here T is plotted in the logarithmic scale.

IX. CONCLUSIONS AND DISCUSSION

To summarize, we have developed a DMFT formalism and its numerical implementation for computing Rényi entanglement entropy and mutual information in strongly correlated electronic systems described by the Hubbard model. We show that the scaling of the Rényi entropy with subsystem size for an extended subsystem can be used to characterize correlated Fermi liquid metallic state in the half-filled Hubbard model. In particular, we show that the subsystem-size scaling of Rényi entropy follows the entropy to entanglement crossover formula expected from CFT and related arguments even in the presence of strong electronic correlations captured by local self-energy approximation within the single-site DMFT. We also show how the first-order Mott transition and Mott critical point are manifested in the temperature, interaction, and subsystem-size dependence of Rényi mutual information.

Here, as a first attempt to implement the entanglement path integral formalism of Ref. [34] within DMFT, we use an approximate impurity solver, namely the IPT [40]. An immediate extension of our work would be to employ the CTQMC impurity solver [48] in the entanglement DMFT framework. Our entanglement path integral formalism is naturally suited for such a purpose and only requires the incorporation of the local kick self-energy [Eqs. (23) and (24)] in the impurity action for the CTQMC solver [48]. Another interesting, albeit more challenging, future direction would be to capture short-range correlations via cluster extension [41,44] of the DMFT formalism. On a different note, it will be interesting to explore the connections between real-space and momentum-space [81] entanglement in a Fermi liquid.

While in this work we have discussed the implementation of the entanglement path integral under equilibrium conditions, the entanglement integral and the DMFT can be extended to nonequilibrium situations, like in the usual nonequilibrium DMFT [42], via the Schwinger-Keldysh formalism as discussed in Refs. [34,35]. Moreover, the nonequilibrium formulation can be further generalized to incorporate nonunitary dynamics, e.g., the dynamics and the steady states of the Hubbard model under repeated projective or weak measurements, to study entanglement transitions similar to that seen in random quantum circuits [82].

In recent years, DMFT, with its integration with other first-principles electronic structure methods [41], has become one of the most practical approaches to describe realistic strongly correlated systems. Thus our DMFT formulations, along with its possible extensions discussed above, might lead to a viable route to computing entanglement properties of strongly correlated materials in the future.

ACKNOWLEDGMENTS

We acknowledge useful discussions with Vijay Shenoy and Siddhartha Lal. S.B. acknowledges support from SERB (CRG/2022/001062), DST, India and QuST, DST, India. A.H. acknowledges the support from SERB (SRG/2023/000118), DST, India.

APPENDIX A: NUMERICAL SOLUTION OF THE DMFT EQUATIONS

The DMFT equations [Eqs. (24)–(26), (28), (29), and (31)] for computing $S_A^{(2)}$ are numerically much more challenging to solve compared to usual equilibrium DMFT equations [40] since the Green's function $G_{i\sigma\alpha,j\sigma\beta}(\tau, \tau')$ [Eq. (18)] is a matrix in both space and time. The space translation symmetry is broken by the entanglement cut, and the time translation symmetry is broken by choice of time τ_0 for inserting the auxiliary fields in the path integral [Eq. (9)]. However, for the cylindrical subsystem geometry in Fig. 5, considered for the 2d Hubbard model, the system retains the translation symmetry parallel to the (y) direction of the entanglement cut. In this case, one can use Fourier transform along the y direction, as we discuss later.

To solve the DMFT equations in imaginary time τ without time-translation invariance, we discretize the DMFT equations in imaginary time. We divide the time interval $[0, \beta)$ at inverse temperature $\beta = 1/T$ into N_τ segments with the discretization step $\delta\tau = \beta/N_\tau$. However, while discretizing we have to ensure the appropriate antiperiodic boundary conditions on the fermionic Green's function, namely,

$$G(\tau + \beta, \tau') = -G(\tau, \tau'), \tag{A1a}$$

$$G(\tau, \tau' + \beta) = -G(\tau, \tau'), \tag{A1b}$$

which is equivalent to the antiperiodic boundary conditions on Grassmann variables, $c_{N_\tau} = -c_0$ and $\bar{c}_{N_\tau} = -\bar{c}_0$, in the time-discretized form. Here we have suppressed the space, spin and replica indices for brevity. We use the indices (n, m) running from $n, m = 0$ to N_τ for (τ, τ'). We also write the following useful discretization rules:

$$(\partial_\tau \bar{c}(\tau))c(\tau) = \frac{(\bar{c}_{n+1} - \bar{c}_n)c_n}{\delta\tau}, \tag{A2a}$$

$$\bar{c}(\tau)c(\tau) = \bar{c}_{n+1}c_n. \tag{A2b}$$

The above rules arise since the creation operator $\bar{c}$ always appears slightly later in time than the annihilation operator c in the path integral. Using the above rules, e.g., we can write

Eq. (20) as

$$S_\lambda = \delta\tau^2 \sum_{n,m=1}^{N_\tau} \sum_{ij,\sigma,\alpha\beta,nm} \bar{c}_{i\sigma\alpha n}\big[-G^{-1}_{0,i\alpha n,j\beta m}\big]c_{j\sigma\beta m} + U\delta\tau \sum_{n=1}^{N_\tau}\sum_{i\alpha} \bar{c}_{i\uparrow\alpha,n+1}c_{i\uparrow\alpha n}\bar{c}_{i\downarrow\alpha,n+1}c_{i\downarrow\alpha n}. \quad \text{(A3)}$$

The inverse of lattice Green's function appearing above is given by

$$-G^{-1}_{0,i\alpha n,j\beta m} = g^{-1}_{\alpha m,\beta n}\delta_{ij} + \frac{1}{\delta\tau}t_{ij}\zeta_{mn}\delta_{\alpha\beta} + \lambda\delta_{i\in A}\delta_{ij}M_{\alpha\beta}\frac{\delta_{m,p+1}\delta_{np}}{\delta\tau^2}, \quad \text{(A4)}$$

where the index $p \in [0, N_\tau)$ is arbitrary depending on τ_0. Here

$$g^{-1}_{\alpha m,\beta n} = \frac{1}{\delta\tau^2}(\zeta_{mn} - \delta_{mn})\delta_{\alpha\beta} - \mu\frac{1}{\delta\tau}\zeta_{mn}\delta_{\alpha\beta} \quad \text{(A5a)}$$

with

$$\zeta_{mn} = \delta_{m,n+1} \quad n < N_\tau$$
$$= -1 \quad m = 1, n = N_\tau. \quad \text{(A5b)}$$

Similarly, Eq. (24) becomes

$$\mathcal{G}^{-1}_{i\alpha m,\beta n} = g^{-1}_{\alpha m,\beta n} - \Delta_{i\alpha m,\beta n} - \lambda\delta_{i\in A}M_{\alpha\beta}\frac{\delta_{m,p+1}\delta_{np}}{\delta\tau^2}. \quad \text{(A6)}$$

The IPT self-energy [Eq. (26)] is obtained as

$$\Sigma_{i\alpha m,\beta n} = UG_{i\alpha m,\beta n}\frac{\delta_{m,n-1}}{\delta\tau} - U^2\tilde{\mathcal{G}}^2_{i\alpha m,\beta n}\tilde{\mathcal{G}}_{i\beta m,\alpha n}, \quad \text{(A7a)}$$

where

$$\tilde{\mathcal{G}}_{i\alpha m,\beta n} = \mathcal{G}_{i\alpha m,\beta n} - UG_{ii,\alpha m,\beta n}\frac{\delta_{m,n-1}}{\delta\tau}. \quad \text{(A7b)}$$

The lattice Green's function is obtained as

$$\sum_{n_1}\sum_{k\gamma} G^{-1}_{i\alpha m,k\gamma n_1}G_{k\gamma n_1,j\beta n} = \delta_{ij}\delta_{\alpha\beta}\frac{\delta_{mn}}{\delta\tau^2}, \quad \text{(A8a)}$$

where within the local self-energy approximation, the Dyson equation is

$$G^{-1}_{i\alpha m,j\beta n} = G^{-1}_{0,i\alpha m,j\beta n} - \delta_{ij}\Sigma_{i\alpha m,\beta n}. \quad \text{(A8b)}$$

Now one can obtain the lattice Green's function from the above equation. The lattice Green's function determines the hybridization function through Eqs. (29) and (30).

1. Recursive Green's function method

The most computationally expensive part of the DMFT steps discussed above is the inversion of G^{-1}, a matrix of dimension $\sim N_xN_\tau \times N_xN_\tau$, to obtain G via Eq. (A8a) for a lattice with N_x sites along the (x) direction of partitioning. A direct inverse with the DMFT self-consistency loop is only feasible for relatively small systems of size $N_x \lesssim 12$ with $N_\tau \lesssim 1000$. For larger systems, we use a recursive Green's function method along the x direction. The recursive method can be implemented for the open boundary condition (OBC) as well as for the periodic boundary condition (PBC). In dimension $d > 1$ with translation symmetry, we can make simplifications by using Fourier transform in the transverse momenta (see the discussion later). To demarcate between directions with translation symmetry and the direction of recursion x, we denote the lattice sites by $\boldsymbol{i} = (i, \boldsymbol{i}_\perp)$ below.

To set up the recursive method, we rewrite Eq. (A8a) as a matrix equation

$$\mathbf{G^{-1}G} = \mathbf{I}, \quad \text{(A9a)}$$
$$\mathbf{I}_{i\alpha m,j\beta n} = \delta_{ij}\delta_{mn}\delta_{\alpha\beta}, \quad \text{(A9b)}$$

where

$$(\mathbf{G})_{i\alpha m,j\beta n} = \delta\tau G_{i\alpha m,j\beta n}, \quad \text{(A9c)}$$

and similarly for $\mathbf{G^{-1}}$. We separate the system (spatially) as a system "S" and the rest "R" and write

$$\begin{bmatrix}(\mathbf{G}_R)^{-1} & -\mathbf{T}_{RS}\\ -\mathbf{T}_{RS} & (\mathbf{G}_S)^{-1}\end{bmatrix}\begin{pmatrix}\mathbf{G}_R^{R+S} & \mathbf{G}_{RS}^{(R+S)}\\ \mathbf{G}_{SR}^{(R+S)} & \mathbf{G}_S^{(R+S)}\end{pmatrix} = \mathbf{I}. \quad \text{(A10)}$$

Here $\mathbf{G}_R$ and $\mathbf{G}_S$ are Green's functions of the system and the rest in the absence of any coupling between them. $\mathbf{T}$ connects the systems and the rest, and $\mathbf{G}^{(R+S)}$ is the full Green's function of the combined system. From the above, we get

$$\mathbf{G}_R^{(R+S)} = \mathbf{G}_R + \mathbf{G}_R\mathbf{T}_{RS}\mathbf{G}_{SR}^{(R+S)}, \quad \text{(A11a)}$$
$$\mathbf{G}_{RS}^{(R+S)} = \mathbf{G}_R\mathbf{T}_{RS}\mathbf{G}_S^{(R+S)}, \quad \text{(A11b)}$$
$$\mathbf{G}_{SR}^{(R+S)} = \mathbf{G}_S\mathbf{T}_{RS}^\dagger\mathbf{G}_R^{(R+S)}, \quad \text{(A11c)}$$
$$\mathbf{G}_S^{(R+S)} = \mathbf{G}_S + \mathbf{G}_S\mathbf{T}_{RS}^\dagger\mathbf{G}_{RS}^{(R+S)}. \quad \text{(A11d)}$$

a. Derivation of Eq. (30) for the cavity Green's function

For this case, we take S as a single site i and R as rest of the system. Using Eqs. (A11a) and (A11b), we obtain

$$\mathbf{G}_R = \mathbf{G}_R^{(R+S)} - \mathbf{G}_{RS}^{(R+S)}\big(\mathbf{G}_S^{(R+S)}\big)^{-1}\mathbf{G}_{SR}^{(R+S)}. \quad \text{(A12)}$$

The above leads to Eq. (30) when we identify $\mathbf{G}^{(i)} = \mathbf{G}_R$, i.e., the cavity Green's function with ith site removed, and $\mathbf{G} = \mathbf{G}^{(R+S)}$, the Green's function of the whole lattice.

b. Recursive solution of Eq. (A9)

We imagine successively building the system along the x direction from the left, starting from the first layer at $i = l = 1$ and then adding successive layers till $l = N_x$. Imagine that at the l-th step of recursion, we have only left $l + 1$ layers, and we separate the system into left l layers ("L"), i.e., R of the preceding section, and add one layer (system "S") more. We denote the Green's function of the left l layers as $\mathbf{G}^{(l)}$ and that of $l + 1$ layers as $\mathbf{G}^{(l+1)}$. From Eqs. (A9)

$$\begin{bmatrix}(\mathbf{G}_L^{(l)})^{-1} & -\mathbf{T}_{LS}\\ -\mathbf{T}_{LS}^\dagger & (\mathbf{G}_S)^{-1}\end{bmatrix}\begin{pmatrix}\mathbf{G}_L^{(l+1)} & \mathbf{G}_{LS}^{(l+1)}\\ \mathbf{G}_{SL}^{(l+1)} & \mathbf{G}_S^{(l+1)}\end{pmatrix} = \mathbf{I}, \quad \text{(A13)}$$

where the coupling between L and S is given by

$$\mathbf{T}_{i,j} = \boldsymbol{\zeta}t_{i,j} \quad i \leqslant l,\ j = l+1$$
$$= 0 \quad \text{otherwise}, \quad \text{(A14a)}$$

with

$$\boldsymbol{\zeta}_{\alpha n,\beta m} = \zeta_{nm}\delta_{\alpha\beta}. \quad \text{(A14b)}$$

The inverse Green's functions of L and S in the absence of any coupling between them are

$$\left(\mathbf{G}_L^{(l)}\right)^{-1}_{i\alpha m,j\beta n} = \mathbf{G}^{-1}_{i\alpha m,j\beta n} \quad i,j \leqslant l, \tag{A14c}$$

$$(\mathbf{G}_S)^{-1}_{i\alpha m,j\beta n} = \mathbf{G}^{-1}_{i\alpha m,j\beta n} \quad i,j = l+1. \tag{A14d}$$

Here $i \leqslant l$ indicates that the site $\boldsymbol{i}$ belongs to a layer from 1 to l. The full Green's function that we eventually want to calculate is $\mathbf{G} = \mathbf{G}^{(N_x)}$. We can rewrite Eq. (A13) as

$$\mathbf{G}_L^{(l+1)} = \mathbf{G}_L^{(l)} + \mathbf{G}_L^{(l)}\mathbf{T}_{LS}\mathbf{G}_{SL}^{(l+1)}, \tag{A15a}$$

$$\mathbf{G}_{LS}^{(l+1)} = \mathbf{G}_L^{(l)}\mathbf{T}_{LS}\mathbf{G}_S^{(l+1)}, \tag{A15b}$$

$$\mathbf{G}_{SL}^{l+1} = \mathbf{G}_s\mathbf{T}_{SL}^{\dagger}\mathbf{G}_L^{(l+1)}, \tag{A15c}$$

$$\mathbf{G}_S^{(l+1)} = \mathbf{G}_S + \mathbf{G}_S\mathbf{T}_{LS}^{\dagger}\mathbf{G}_{LS}^{(l+1)}. \tag{A15d}$$

We now rewrite Eq. (A15a) keeping only the index i for the layers, where all other indices α, m and $\boldsymbol{i}_\perp$ are implicit in the matrices and contracted for matrix multiplications.

$$\mathbf{G}_{i,j}^{(l+1)} = \mathbf{G}_{i,j}^{(l)} + \sum_{i_1 \leqslant l} \mathbf{G}_{i,i_1}^{(l)}\mathbf{T}_{i_1,l+1}\mathbf{G}_{l+1,j}^{(l+1)} \quad i,j \leqslant l. \tag{A16}$$

From Eq. (A15b), we get

$$\mathbf{G}_{i,l+1}^{(l+1)} = \sum_{i_1 \leqslant l} \mathbf{G}_{i,i_1}^{(l)}\mathbf{T}_{i_1,l+1}\mathbf{G}_{l+1,l+1}^{(l+1)} \quad i \leqslant l. \tag{A17}$$

Since $G^*_{i\alpha m,j\beta n} = G_{j\beta n,i\alpha m}$, we can obtain from the above

$$\mathbf{G}_{l+1,i}^{(l+1)} = \sum_{i_1 \leqslant l} \mathbf{G}_{l+1,l+1}^{(l+1)}\mathbf{T}_{l+1,i_1}\mathbf{G}_{i_1,i}^{(l)} \quad i \leqslant l. \tag{A18}$$

Using the above in Eq. (A16), we obtain for $i, j \leqslant l$

$$\mathbf{G}_{i,j}^{(l+1)} = \mathbf{G}_{i,j}^{(l)} + \sum_{i_1,i_2 \leqslant l} \mathbf{G}_{i,i_1}^{(l)}\mathbf{T}_{i_1,l+1}\mathbf{G}_{l+1,l+1}^{(l+1)}\mathbf{T}_{l+1,i_2}\mathbf{G}_{i_2,j}^{(l)}. \tag{A19}$$

In the above equation, the only unknown quantity is $\mathbf{G}_{l+1,l+1}^{(l+1)}$. This can be obtained as follows. From Eqs. (A15b) and (A15d), we get

$$\mathbf{G}_S^{(l+1)} = \mathbf{G}_S + \mathbf{G}_S\mathbf{T}_{LS}^{\dagger}\mathbf{G}_L^{(l)}\mathbf{T}_{LS}\mathbf{G}_S^{(l+1)}. \tag{A20}$$

The above can be written in the form of a Dyson equation,

$$\left(\mathbf{G}_S^{l+1}\right)^{-1} = \left(\mathbf{G}_{l+1,l+1}^{(l+1)}\right)^{-1} = \mathbf{G}_S^{-1} - \mathbf{\Sigma}^{(l)} \tag{A21}$$

with the self-energy

$$\mathbf{\Sigma}^{(l)} = \sum_{i_1,i_2 \leqslant l} \mathbf{T}_{l+1,i_1}\mathbf{G}_{i_1,i_2}^{(l)}\mathbf{T}_{i_2,l+1}. \tag{A22}$$

Hence $\mathbf{G}_{l+1,l+1}^{(l+1)}$ can be obtained using Eq. (A21). Thus from Eqs. (A17)–(A19), (A21), and (A22), we can construct the complete Green's function matrix $\mathbf{G}_{i\alpha m,j\beta n}^{(l+1)}$ $(i,j \leqslant l+1)$ of the system of $l+1$ layers from that of l layers. The process can be applied recursively, starting with $l = 1$ and continuing till $l = N_x - 1$, which will yield us the Green's function of system size N_x, i.e., $\mathbf{G}^{(N_x)}$. However, for the DMFT self-consistency Eqs. (24)–(26), (28), (29), and (31), one does not need the full Green's function at each DMFT iteration, only certain elements. In particular, if we only consider the nearest neighbor hopping, we will need to keep track of the onsite, nearest, and next-nearest neighbor Green's functions to complete the DMFT loop using the cavity Eqs. (29) and (30). For the Bethe lattice approximation, nearest-neighbor sites of ith site are disconnected, and from Eq. (29), we get

$$\Delta_{i,\alpha\beta}(\tau,\tau') = t^2 \sum_j{}' G^{(i)}_{j\alpha,j\beta}(\tau,\tau'). \tag{A23}$$

Here $\sum'_j$ indicates only summation over nearest neighbors of i. Furthermore, in the limit of large connectivity [40], $\mathbf{G}^{(i)} = \mathbf{G}$. Thus, in the large-connectivity Bethe lattice approximation, we only need to compute onsite elements of the lattice Green's function during the DMFT self-consistency loop.

For periodic boundary condition (PBC), we need to incorporate the hopping matrix element between site 1 and site N_x. We can implement this in the recursive procedure by changing the hopping coupling matrix in the last iteration accordingly when we add the $l = N_x - 1$ layer with a single layer system S to form the required system size $l+1 = N_x$. In particular, we can explicitly write the hopping coupling matrix for the nearest neighbor for PBC below

$$\begin{aligned}\mathbf{T}_{i,j} &= \zeta t_{i,j} \quad i = l; j = l+1 \ \text{ if } \ l \leqslant N_x - 2\\ &= \zeta t_{i,j} \quad i = 1, l; j = l+1 \ \text{ if } \ l = N_x - 1\\ &= 0 \quad \text{otherwise,}\end{aligned} \tag{A24}$$

APPENDIX B: CALCULATION OF $S_A^{(2)}$ FROM "KICK TERM" INTEGRATION METHOD

We numerically solve the self-consistent DMFT Eqs. (A6), (A7a), (A8a), and (29) for discretized values of $\lambda \in [0,1]$ with uniform step $\delta\lambda$ to obtain $G_{i\sigma\alpha,j\sigma\beta}(\tau_0,\tau_0^+)$ [Eq. (18)], where we choose $\tau_0 = 0$. We then compute $\langle S_{\text{kick}}\rangle_{Z_A^{(2)}(\lambda)}$ using Eq. (17). To obtain $S_A^{(2)}$, we integrate $\langle S_{\text{kick}}\rangle_{Z_A^{(2)}(\lambda)}$ over λ from 0 to 1 using numerical interpolation over the range of λ.

We have used $\delta\lambda = 0.1$ for most of our calculations. We have varied $\delta\lambda$ to check the convergence of $S_A^{(2)}$ with $\delta\lambda$. We benchmark the $S_A^{(2)}$ computed this way in the noninteracting case by comparing with $S_A^{(2)}$ obtained directly from the correlation matrix calculations, as discussed in Sec. V A. For the interacting case, we have numerically checked the convergence by taking different values of $\delta\lambda$, and various numerical interpolation schemes. As an example, in Fig. 15, we show the convergence of the $S_A^{(2)}$ with different $\delta\lambda = 0.02, 0.04, 0.1$, for $U = 2.0$, $T = 0.05$, and $N = 30$ in 1d.

APPENDIX C: BENCHMARK OF THE RECURSIVE GREEN'S FUNCTION METHOD

We can invert $\mathbf{G}^{-1}$ in Eq. (A8a) directly for small systems ($N \lesssim 12$) to obtain the lattice Green's function. We use the recursive method for larger systems to invert $\mathbf{G}^{-1}$ and obtain onsite lattice Green's function within the DMFT loop. We benchmark the recursive method by comparing computed $S_A^{(2)}$ with that obtained from direct inversion for $N = 10$ in 1d, as shown in Fig. 16 for the noninteracting case.

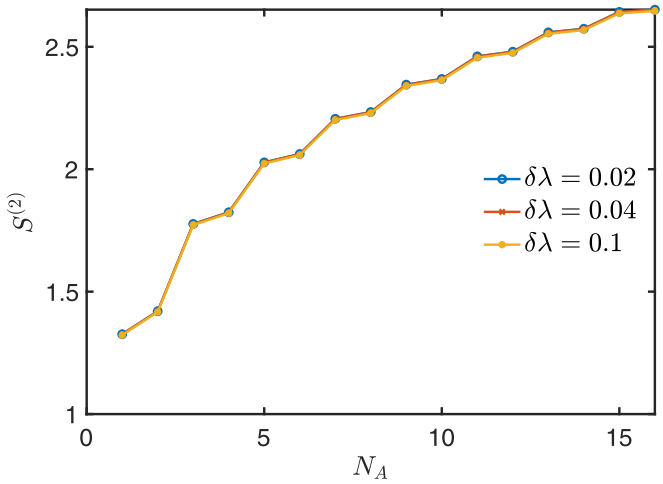

FIG. 15. The convergence of $S_A^{(2)}$ with respect to discretization $\delta\lambda$ to evaluate the integral in Eq. (17) for $U = 2.0$, $T = 0.05$, and system size $N = 30$ in 1d Hubbard model.

APPENDIX D: THE EXTRAPOLATION OF $S_A^{(2)}(\delta\tau)$ TO $\delta\tau \to 0$ LIMIT

As discussed in Appendix A, we solve the DMFT self-consistency equations by discretizing them in imaginary time with discretization step $\delta\tau = \beta/N_\tau$. To approach the continuum limit $\delta\tau \to 0$, we compute $S_A^{(2)}(\delta\tau)$ for a few values $\delta\tau$ and then linearly extrapolate it to $\delta\tau \to 0$. We take $\delta\tau$ over the range 0.015 to 0.075. In most of our calculations, we take four values of $\delta\tau$ in the above range, particularly between 0.02 to 0.04, and then do the linear extrapolation to $\delta\tau \to 0$. It becomes progressively more challenging to take $\delta\tau$ in the above range for low temperatures $T < 0.05$ as the size $(2NN_\tau \times 2NN_\tau)$ of the Green's function matrix becomes very large. Hence we restrict our DMFT calculations up to $T = 0.05$. We show $S_A^{(2)}(\delta\tau)$ as a function of $\delta\tau$ with the linear extrapolation in Figs. 17(a) and 17(b) for a few subsystem sizes for interactions $U = 0.5,\ 2$ and system size $N = 30$ as an illustration of the linear extrapolation.

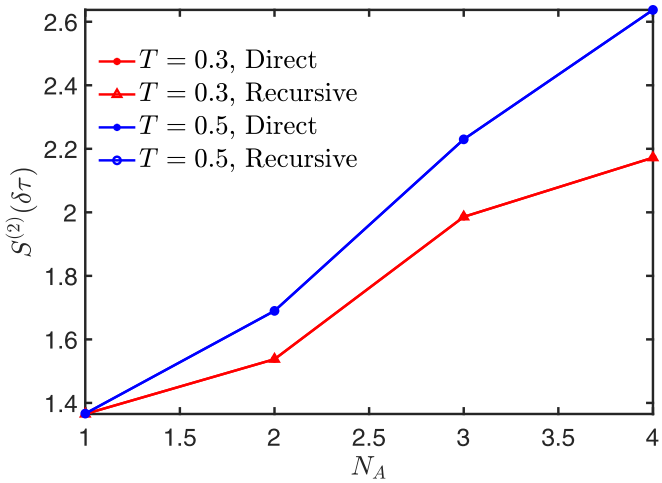

FIG. 16. The $S_A^{(2)}(\delta\tau)$ obtained using the direct and recursive inversion in the noninteracting case is shown for $T = 0.3,\ 0.5$ and system size $N = 10$.

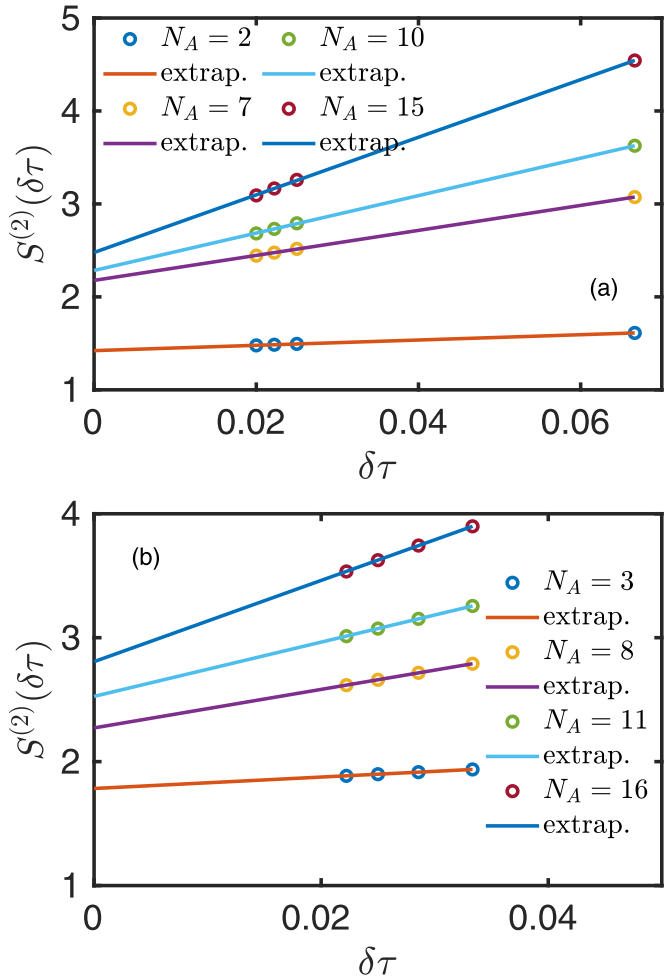

FIG. 17. The linear extrapolations of $S_A^{(2)}(\delta\tau)$ are shown here for few subsystem sizes. The $S_A^{(2)}(\delta\tau)$ as a function of $\delta\tau$ and the corresponding linear extrapolation (shown as "extrap." in legend) are shown here in (a) for $U = 0.5$ and subsystem sizes $N_A = 2,\ 7,\ 10,$ and 15 from system size $N = 30$, and in (b) for $U = 2$ and subsystem sizes $N_A = 3,\ 8,\ 11,$ and 16 from system $N = 50$ for at $T = 0.05$.

APPENDIX E: ENTANGLEMENT TO ENTROPY CROSSOVER IN 1D HUBBARD MODEL

Here we discuss the fitting of $S_A^{(2)}$ in 1d Hubbard model with the crossover function of Eq. (34). We first fit $S_A^{(2)}(N_A, T)$ with Eq. (34) by varying all the parameters c, v, b, as shown in Fig. 18. The variations of the extracted fitting parameters c, v, b with temperature are shown in Fig. 19. As evident from the figure, the expected CFT crossover formula [Eq. (34)] describes $S_A^{(2)}$ for the DMFT metallic state of 1d Hubbard model quite well. The extracted central charge slowly approaches the CFT value $c = 1$ with decreasing temperature [Fig. 19(a)] and converges well with system size N [Fig. 19(d)]. Here we have treated c, v, b in Eq. (34) as fitting parameters to describe $S_A^{(2)}(N_A, T)$ in the 1d Hubbard model. In the next section, we first fix the ratio (c/v) using the specific heat calculated

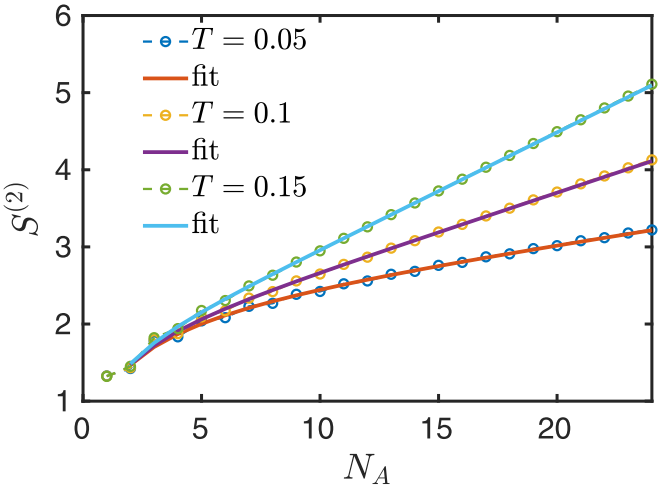

FIG. 18. The $S_A^{(2)}$ vs N_A in 1d Hubbard model for $U = 2$ and $N = 50$ is shown for different temperatures with the corresponding fit to Eq. (34) with c, v, b as free parameters.

from equilibrium DMFT and then fit our results for $S_A^{(2)}$ with Eq. (34) treating only c and b as fitting parameters.

1. Calculation of the ratio (c/v) from equilibrium DMFT

At low temperature ($T \to 0$), the specific heat c_V can be obtained from CFT [8,12] as

$$c_V = \frac{\pi T}{3}\left(\frac{c}{v}\right). \tag{E1}$$

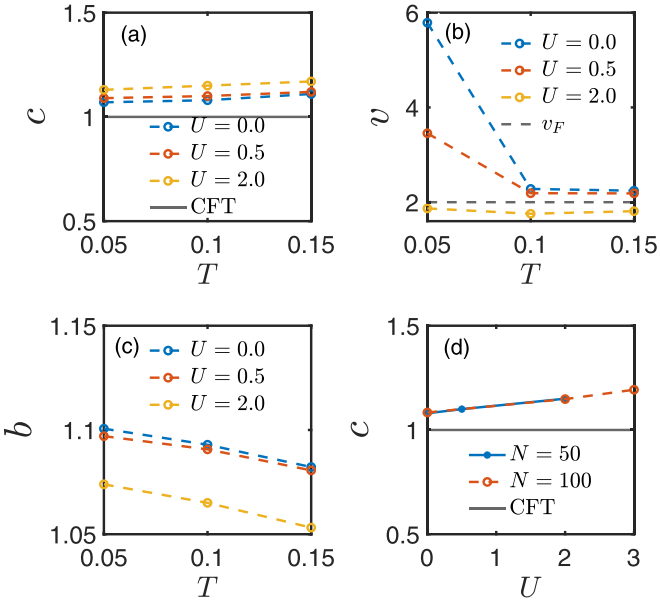

FIG. 19. The parameters c, v, b extracted from crossover function [Eq. (34)] fitting, e.g., in Fig. 18, are shown here for 1d Hubbard model. (a) The central charge c as a function of T for a few U is shown and compared with the CFT value $c = 1$. (b) The renormalized Fermi velocity v as a function of T is shown for different U, and compared with the noninteracting value v_F. (c) The nonuniversal parameter b as a function of T. (d) System size dependence of extracted c vs U at $T = 0.1$.

We compute the specific heat c_V for the paramagnetic metallic state in 1d Hubbard model from equilibrium DMFT calculation, as described below.

In equilibrium, due to time translation symmetry, $G_{ij}(\tau, \tau') = G_{ij}(\tau - \tau')$. Thus we can write the DMFT self-consistency equations [40] as follows:

$$\mathcal{G}_i^{-1}(\tau - \tau') = -(\partial_\tau - \mu)\delta(\tau - \tau') - \Delta_i(\tau - \tau') \tag{E2}$$

$$G_i^{-1}(\tau) = \mathcal{G}_i^{-1}(\tau) - \Sigma_i(\tau), \tag{E3}$$

where $\mathcal{G}_i(\tau)$ and $G_i(\tau)$ are the bare and full impurity Green's functions at site i. Furthermore, since the model [Eq. (19)] is space translation invariant, all the sites are equivalent, unlike for the DMFT in the presence of entanglement cut in Sec. IV.

The hybridization function is given by

$$\Delta_i(\tau) = \sum_{jl} t_{ij} t_{il} G_{jl}^{(i)}(\tau). \tag{E4}$$

We use the large-connectivity Bethe lattice approximation for the cavity Green's function, i.e., $G_{jl}^{(i)} = G_{jl}$, and $G_{jl}^{(i)} \simeq \delta_{jl} G_{jj}$. Therefore the hybridization function for nearest-neighbor hopping becomes

$$\Delta_i(\tau) = z t^2 G(\tau), \tag{E5}$$

where $G(\tau)$ is the onsite lattice Green's function and $z = 2d$ is the coordination number for D-dimensional hypercubic lattice. The lattice Green's function is obtained using the local self-energy approximation, i.e., the lattice self-energy Σ_{ij} is replaced by the impurity self-energy, $\Sigma_{ij} = \Sigma\delta_{ij}$, so that

$$G(i\omega_m) = \int d\epsilon \frac{g(\epsilon)}{\imath\omega_m + \mu - \epsilon - \Sigma(\imath\omega_m)}, \tag{E6}$$

where $\omega_m = (2m + 1)\pi/\beta$, with m an integer, is the fermionic Matsubara frequency, and $g(\epsilon)$ is the noninteracting density of states per site. The self-energy within IPT approximation [40] is given by

$$\Sigma(\tau) = Un - U^2 \tilde{\mathcal{G}}^2(\tau)\tilde{\mathcal{G}}(-\tau), \tag{E7}$$

$$\tilde{\mathcal{G}}^{-1}(\tau) = \mathcal{G}^{-1}(\tau) - Un, \tag{E8}$$

where n is the occupation number of a site; $n = 1/2$ at half filling. For calculating thermodynamic properties such as specific heat, we solve the above equilibrium DMFT self-consistency equation following standard procedure [40] to obtain $G(\imath\omega_m)$ and $\Sigma(\imath\omega_m)$.

Using these, we compute the internal energy E [40] from

$$\frac{E}{N} = 2T \sum_m \int_{-\infty}^{\infty} d\epsilon \frac{\epsilon D(\epsilon)}{i\omega_m + \mu - \Sigma_(i\omega_m) - \epsilon} + T \sum_m \Sigma(i\omega_m) G(i\omega_m). \tag{E9}$$

The specific heat per site is obtained by taking the numerical derivative of internal energy, i.e., $c_V = (1/N)(\partial E/\partial T)$.

We calculate the specific heat as a function of temperature for 1d and 2d Hubbard models. We show c_V versus T in 1d Hubbard model in Fig. 20. We extract (c/v) from the slope of the linear fit to $c_V(T)$ at low temperature using Eq. (E1), as shown in the figure. For the half-filled 2d square-lattice Hubbard model with nearest-neighbor hopping, due to the

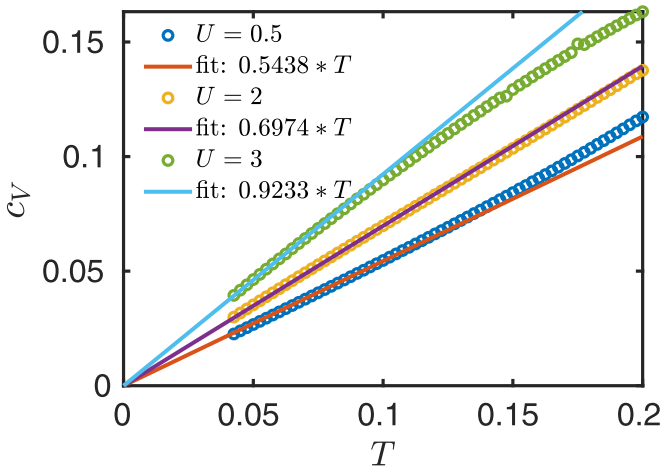

FIG. 20. The specific heat (c_V) as a function of temperature T for 1d Hubbard model is shown for different interaction $U = 0.5,\ 2,$ and 3. The low-temperature linear fit to $c_V(T) \propto T$ is shown and the extracted slopes are indicated in the legends.

van Hove singularity of the noninteracting band at the Fermi energy c_V has $\ln T$ correction to Eq. (E1), and the (c/v) ratio cannot be estimated reliably. Thus we only use the (c/v) ratio in 1d to fit $S_A^{(2)}(N_A, T)$ with the crossover formula [Eq. (34)], as discussed in Sec. VI. The central charge c extracted this way is shown in Fig. 4. We show the nonuniversal constant b and the velocity v, obtained using the (c/v) ratio and c, in Figs. 21(a) and 21(b). As evident, v extracted this way for weak interaction matches quite well at low temperatures with noninteracting v_F, unlike the v extracted by fitting the CFT formula with three parameters $c,\ v,\ b$ in Fig. 19(b). For the 2d

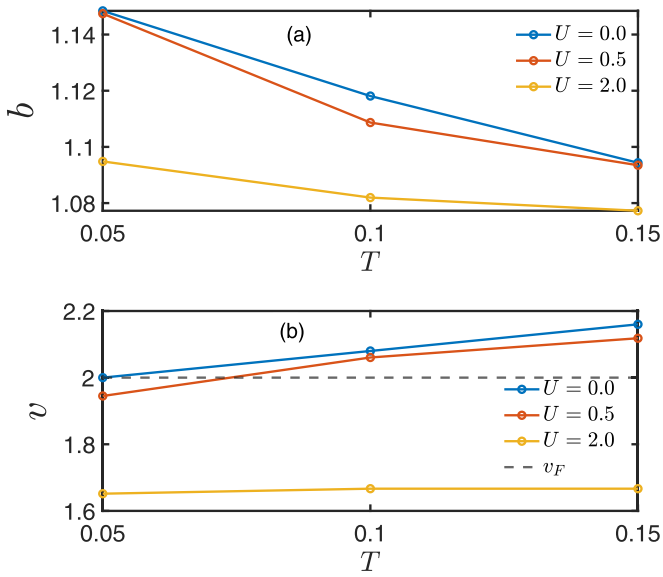

FIG. 21. Temperature dependence of (a) b and (b) v extracted by fixing (c/v) ratio from specific heat and fitting CFT crossover formula [Eq. (34)] to the DMFT results for $S_A^{(2)}(N_A, T)$ in the 1d Hubbard model for $U = 0.0, 0.5, 2$ and system size $N = 50$. The noninteracting Fermi velocity v_F is shown in plot (b) for comparison with renormalized velocity v.

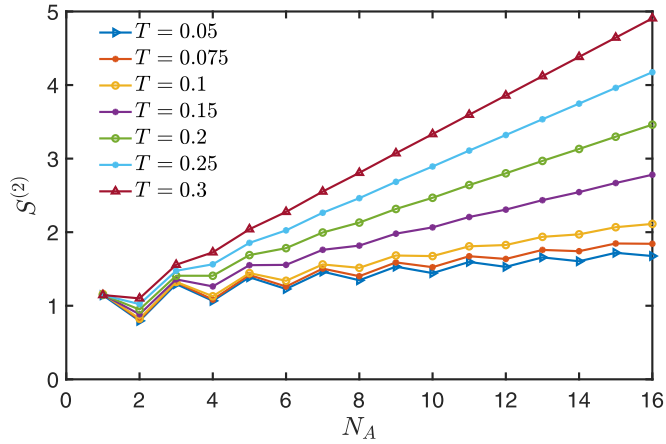

FIG. 22. The $S_A^{(2)}$ as a function of N_A is shown here for different T for open boundary condition (OBC) for $U = 2.0$. The system size is $N = 30$ here.

Hubbard model, we extract c by fitting the crossover formula [Eq. (34)] to the computed $S_A^{(2)}(N_A, T)$ using c, v, b as free parameters, as discussed in Sec. VII.

APPENDIX F: $S_A^{(2)}(N_A, T)$ FOR OPEN BOUNDARY CONDITION (OBC) IN 1D HUBBARD MODEL

We show the second Rényi entropy $S_A^{(2)}$ computed via DMFT for open boundary condition (OBC) in the 1d Hubbard model for system size $N = 30$ in Fig. 22. We see quite large oscillations in $S_A^{(2)}$ between the odd and even subsystem sizes at low temperatures for OBC. Such oscillations are present for periodic boundary condition also, e.g., in Fig. 3, but are much weaker. These oscillations, with frequency $2k_F$ determined by the Fermi wave vector k_F, are expected [83,84] due to the subleading corrections to the CFT result [Eq. (37)], and appear to be enhanced in OBC compared to that in PBC.

APPENDIX G: DMFT EQUATIONS FOR COMPUTING SECOND RÉNYI ENTROPY IN 2d

In two dimensions (2d), we take a cylindrical geometry for the subsystem A to compute the second Rényi entropy, as shown in Fig. 5. We take the entanglement cut parallel to the y axis, i.e., partition the system along the x direction. The most difficult part in solving the nonequilibrium DMFT Eqs. (24)–(26), (28), (29), and (31) is the inversion of the inverse lattice Green's function. We rewrite Eq. (28) below as

$$\int_0^\beta d\tau'' \sum_{\boldsymbol{r}''\gamma} [G^{-1}_{0,\boldsymbol{r}\alpha,\boldsymbol{r}''\gamma}(\tau,\tau'') - \delta_{\boldsymbol{r},\boldsymbol{r}''}\Sigma_{\boldsymbol{r},\alpha\gamma}(\tau,\tau'')] G_{\boldsymbol{r}''\gamma,\boldsymbol{r}'\beta}(\tau'',\tau') = \delta_{\boldsymbol{r},\boldsymbol{r}'}\delta_{\alpha\beta}\delta(\tau-\tau'), \tag{G1}$$

where $\boldsymbol{r} = (x, y)$ represents two dimensional co-ordinates. Due to translation symmetry in the y direction, $G_{\boldsymbol{r}\alpha,\boldsymbol{r}'\beta}(\tau,\tau') = G_{x\alpha,x'\beta,y-y'}(\tau,\tau')$. As a result, Green's function can be represented using Fourier transform along the

y direction with momentum k_y,

$$G_{x\alpha,x'\beta,y-y'}(\tau,\tau') = \frac{1}{N_y}\sum_{k_y} e^{-ik_y(y-y')} G_{x\alpha,x'\beta,k_y}(\tau,\tau'). \quad \text{(G2)}$$

Thus, from Eq. (G1), we can write

$$\int_0^\beta d\tau'' \sum_{x''\gamma} \left[G^{-1}_{0,x\alpha,x''\gamma,k_y}(\tau,\tau'') - \delta_{xx''}\Sigma_{x,\alpha\gamma}(\tau,\tau'')\right] \times G_{x''\gamma,x'\beta,k_y}(\tau'',\tau') = \delta_{xx'}\delta_{\alpha\beta}\delta(\tau-\tau') \quad \text{(G3)}$$

for each k_y mode, where

$$G^{-1}_{0,x\alpha,x'\gamma,k_y}(\tau,\tau') = [(-\partial_\tau + \mu - 2t\cos k_y)\delta_{xx'} - t_{xx'}]\delta_{\alpha\beta}\delta(\tau-\tau'), \quad \text{(G4)}$$

where $t_{xx'}$ is hopping amplitude along x direction. For nearest-neighbor hopping, we have $t_{x,x\pm1} = t$, and $t_{xx'} = 0$ otherwise. The hybridization function with large-connectivity Bethe lattice approximation is given by

$$\Delta_{x,\alpha\beta} = t^2[G_{x-1,\alpha,x-1,\beta,y-y'=0} + G_{x+1,\alpha,x+1,\beta,y-y'=0} + 2G_{x\alpha,x\beta,y-y'=0}]. \quad \text{(G5)}$$

In the above equation, we have omitted the time arguments (τ,τ') for notational convenience. The Green's function $G_{x\alpha,x\beta,y-y'=0}(\tau,\tau')$ is obtained from Eq. (G2) as

$$G_{x\alpha,x\beta,y-y'=0}(\tau,\tau') = \frac{1}{N_y}\sum_{k_y} G_{x\alpha,x\beta,k_y}(\tau,\tau'). \quad \text{(G6)}$$

We use the recursive Green's function method in the x direction for $G_{x\alpha,x\beta,k_y}(\tau,\tau')$, as described in Appendix A, to obtain the lattice Green's function for each k_y mode.

APPENDIX H: WIDOM FORMULA FOR $S_A^{(2)}(N_A, T)$ IN 2d

As we discussed in the main text, in the Widom formula, the effective number of modes from Fermi surface assuming made of independent patches is given by Eq. (35) and we rewrite it here

$$N_{\text{modes}} = \frac{1}{(2\pi)^{d-1}}\frac{1}{2}\int_{\partial A_x}\int_{\partial A_k} dA_x dA_k |\hat{\boldsymbol{n}}_x\cdot\hat{\boldsymbol{n}}_k|. \quad \text{(H1)}$$

We use the 2d noninteracting dispersion $\varepsilon_k = -2t\cos k_x - 2t\cos k_y$ for nearest neighbor hopping. The Fermi surface at half filling is shown in Fig. 23. The unit normal to Fermi-surface $\hat{\boldsymbol{n}}_k = \frac{1}{\sqrt{2}}(\pm\hat{x}\pm\hat{y})$. For cylindrical geometry, we have two interfaces parallel to y axis and hence the unit normal to real space $\hat{\boldsymbol{n}}_x = \pm\hat{x}$. Hence, we get $|\hat{\boldsymbol{n}}_k\cdot\hat{\boldsymbol{n}}_x| = \frac{1}{\sqrt{2}}$. Therefore

$$N_{\text{modes}} = \frac{1}{4\pi}\times 2N_y \times (4\sqrt{2}\pi)\times\frac{1}{\sqrt{2}} = 2N_y, \quad \text{(H2)}$$

where the contribution $2N_y$ comes from integration over real space boundary and $4\sqrt{2}\pi$ comes from integration over the Fermi-surface.

We fit the numerically computed $S^{(2)}/N_y$ data within DMFT to the Widom crossover formula Eq. (37) and the extracted central charge c as a function of T, U and system size are shown in the main text. In Fig. 24, the temperature dependence of renormalized velocity v and nonuniversal constant b extracted by fitting to Eq. (37) are shown for different interaction U. These parameters (v, b) are shown for system 20×20.

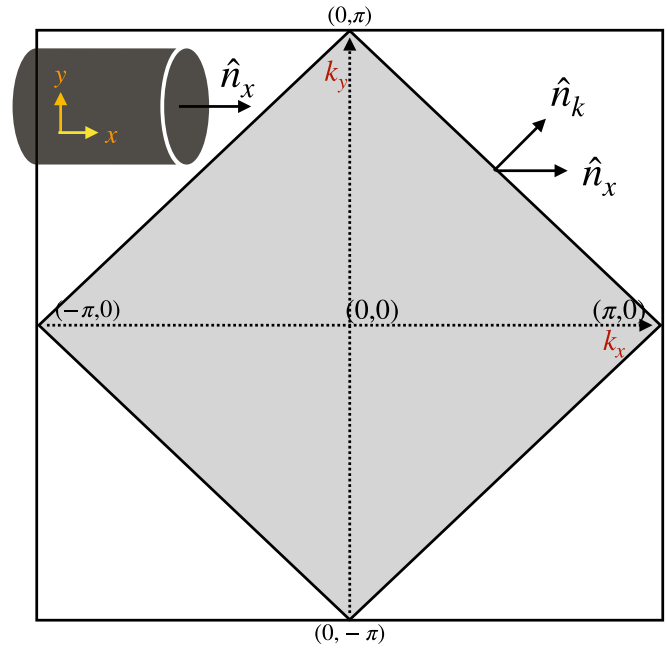

FIG. 23. A schematic of the Fermi sea at half-filling (in gray color) for noninteracting 2d tight-binding model. The real-space subsystem of cylindrical geometry is shown in the top left corner. $\hat{n}_k$ is a unit vector perpendicular to Fermi surface and $\hat{n}_x$ is perpendicular to real-space boundaries of the subsystem.

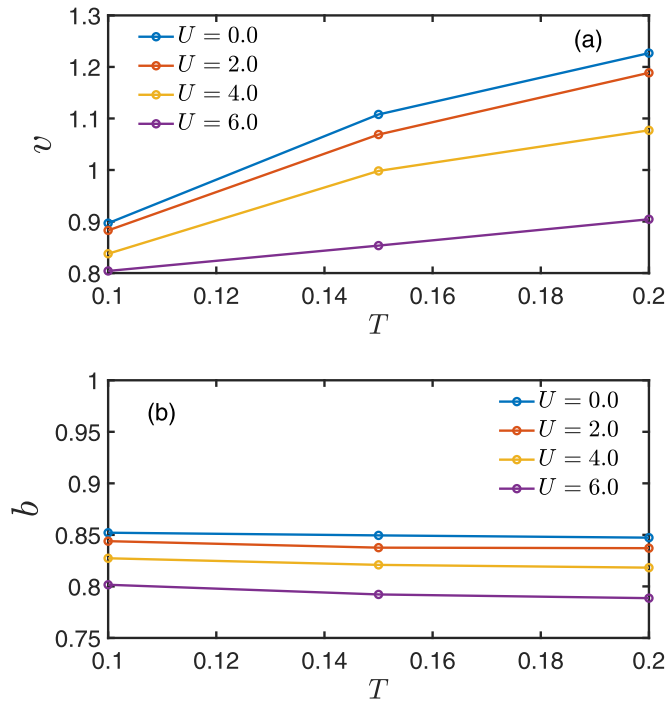

FIG. 24. The temperature dependence of (a) v and (b) b extracted by fitting Widom crossover formula of Eq. (37) to $S^{(2)}/N_y$ for different U computed from system size 20×20.

APPENDIX I: RÉNYI ENTROPY IN ANTIFERROMAGNETIC PHASE

In this work, we have only considered paramagnetic Mott insulating state to make the numerical computation of subsystem Rényi entropy simpler. However, the paramagnetic state is not expected to be a true ground state in the Mott insulating phase, at least not for unfrustrated lattices like square lattice [40]. The ground-state of the Mott insulating phase is expected to Néel-type antiferromagnetic order with two-sublattice ordering for the bipartite square lattice considered here.

We can readily extend our DMFT formalism for entanglement to study the antiferromagnetic long-range order in the Hubbard model. The Néel antiferromagnetic state at half filling has a wave vector $\boldsymbol{Q} = (\pi, \pi)$ for 2d square lattice. As a result, we have two inequivalent sublattices A (namely, site i) and B (nearest-neighbor site j to site i) whose spins like to antialign with each other. As a result, each sublattice prefers one of the spin components over the other. Hence, the local Green's functions for the spin up ($G_{i\uparrow}$) and down ($G_{i\downarrow}$) are not equivalent. Instead, we have the following relation in equilibrium:

$$G_{A;i,\sigma}(\mathrm{i}\omega_n) = G_{B;j,-\sigma}(\mathrm{i}\omega_n), \tag{I1}$$

where $\sigma = \uparrow, \downarrow$ and i and j are nearest neighbors. The Weiss function for sublattice A reads as

$$\mathcal{G}^{-1}_{0,i,\sigma}(\mathrm{i}\omega_n) = \mathrm{i}\omega_n + \mu - \Delta_{i,\sigma}(\mathrm{i}\omega_n), \tag{I2}$$

where the hybridization function within large connectivity Bethe-lattice approximation is given by

$$\Delta_{i,\sigma}(\mathrm{i}\omega_n) = t^2 \sum_j{}' G_{j,\sigma}(\mathrm{i}\omega_n) = zt^2 G_{i,-\sigma}(\mathrm{i}\omega_n). \tag{I3}$$

Now, we can generalize the above relation for our nonequilibrium inhomogeneous DMFT for the entanglement action. The Weiss field for spin σ is given by

$$\begin{aligned}\mathcal{G}^{-1}_{i,\sigma}(\tau,\tau') = &-(\partial_\tau - \mu)\delta(\tau-\tau')\mathcal{I} - \Delta_{i,\sigma}(\tau,\tau') \\ &- \delta_{i\in A} M\delta(\tau-\tau_0^+)\delta(\tau'-\tau_0),\end{aligned} \tag{I4}$$

where $\mathcal{G}^{-1}_{i\sigma}(\tau,\tau')$ is a 2×2 matrix in the entanglement replica space, and $\mathcal{I}$ is the identity matrix in the same space. The hybridization function within the large connectivity Bethe-lattice approximation is given by

$$\begin{aligned}\Delta_{i\sigma,\alpha\beta}(\tau,\tau') &= t^2 \sum_j{}' G_{j\sigma\alpha,j\sigma\beta}(\tau,\tau') \\ &= zt^2 G_{i,-\sigma,\alpha;i,-\sigma,\beta}(\tau,\tau'),\end{aligned} \tag{I5}$$

where $\sum_j'$ indicates that the summation is over only the nearest neighbors of i. As before, the impurity Green's function is related to the Wiess field via the Dyson equation,

$$G^{-1}_{i\sigma}(\tau,\tau') = \mathcal{G}^{-1}_{i\sigma}(\tau,\tau') - \Sigma_{i\sigma}(\tau,\tau'). \tag{I6}$$

The IPT self-energy is given by

$$\begin{aligned}\Sigma_{i\sigma,\alpha\beta}(\tau,\tau') = &\, U G_{i\sigma,i\sigma,\alpha\beta}(\tau,\tau^+)\delta(\tau'-\tau^+)\delta_{\alpha\beta} \\ &- U^2 \tilde{\mathcal{G}}_{i\sigma;\beta\alpha}(\tau,\tau')\tilde{\mathcal{G}}_{i,-\sigma;\beta\alpha}(\tau,\tau')\tilde{\mathcal{G}}_{i,-\sigma;\alpha\beta}(\tau',\tau).\end{aligned} \tag{I7}$$

Here the first term is Hartree self-energy, and the second one is the second-order self-energy obtained using Hartree corrected Green's function

$$\begin{aligned}\tilde{\mathcal{G}}^{-1}_{i\sigma,\alpha\beta}(\tau,\tau') = &\, \mathcal{G}^{-1}_{i\sigma,\alpha\beta}(\tau,\tau') \\ &- U G_{i\sigma,i\sigma,\alpha\beta}(\tau,\tau^+)\delta(\tau'-\tau^+)\delta_{\alpha\beta}.\end{aligned} \tag{I8}$$

[1] M. A. Nielsen and I. L. Chuang, *Quantum Computation and Quantum Information* (Cambridge University Press, 2000).

[2] N. Laflorencie, Quantum entanglement in condensed matter systems, Phys. Rep. **646**, 1 (2016).

[3] M. Levin and X.-G. Wen, Detecting topological order in a ground state wave function, Phys. Rev. Lett. **96**, 110405 (2006).

[4] A. Kitaev and J. Preskill, Topological entanglement entropy, Phys. Rev. Lett. **96**, 110404 (2006).

[5] R. Nandkishore and D. A. Huse, Many-body localization and thermalization in quantum statistical mechanics, Annu. Rev. Condens. Matter Phys. **6**, 15 (2015).

[6] E. Altman and R. Vosk, Universal dynamics and renormalization in many-body-localized systems, Annu. Rev. Condens. Matter Phys. **6**, 383 (2015).

[7] D. A. Abanin, E. Altman, I. Bloch, and M. Serbyn, Colloquium: Many-body localization, thermalization, and entanglement, Rev. Mod. Phys. **91**, 021001 (2019).

[8] P. Calabrese and J. Cardy, Entanglement entropy and quantum field theory, J. Stat. Mech.: Theory Exp. (2004) P06002.

[9] G. Vidal and R. F. Werner, Computable measure of entanglement, Phys. Rev. A **65**, 032314 (2002).

[10] J. Eisert, M. Cramer, and M. B. Plenio, Colloquium: Area laws for the entanglement entropy, Rev. Mod. Phys. **82**, 277 (2010).

[11] H. Casini and M. Huerta, Entanglement entropy in free quantum field theory, J. Phys. A: Math. Theor. **42**, 504007 (2009).

[12] V. E. Korepin, Universality of entropy scaling in one dimensional gapless models, Phys. Rev. Lett. **92**, 096402 (2004).

[13] D. Gioev and I. Klich, Entanglement entropy of fermions in any dimension and the widom conjecture, Phys. Rev. Lett. **96**, 100503 (2006).

[14] W. Li, L. Ding, R. Yu, T. Roscilde, and S. Haas, Scaling behavior of entanglement in two- and three-dimensional free-fermion systems, Phys. Rev. B **74**, 073103 (2006).

[15] B. Swingle, Entanglement entropy and the fermi surface, Phys. Rev. Lett. **105**, 050502 (2010).

[16] B. Swingle, Conformal field theory approach to fermi liquids and other highly entangled states, Phys. Rev. B **86**, 035116 (2012).

[17] B. Swingle, Rényi entropy, mutual information, and fluctuation properties of fermi liquids, Phys. Rev. B **86**, 045109 (2012).

[18] B. Swingle and T. Senthil, Universal crossovers between entanglement entropy and thermal entropy, Phys. Rev. B **87**, 045123 (2013).

[19] P. Calabrese and J. Cardy, Entanglement entropy and conformal field theory, J. Phys. A: Math. Gen. **42**, 504005 (2009).

[20] M. B. Hastings, I. González, A. B. Kallin, and R. G. Melko, Measuring Renyi entanglement entropy in quantum Monte Carlo simulations, Phys. Rev. Lett. **104**, 157201 (2010).

[21] S. Humeniuk and T. Roscilde, Quantum Monte Carlo calculation of entanglement rényi entropies for generic quantum systems, Phys. Rev. B **86**, 235116 (2012).

[22] T. Grover, Entanglement of interacting fermions in quantum Monte Carlo calculations, Phys. Rev. Lett. **111**, 130402 (2013).

[23] F. F. Assaad, T. C. Lang, and F. Parisen Toldin, Entanglement spectra of interacting fermions in quantum Monte Carlo simulations, Phys. Rev. B **89**, 125121 (2014).

[24] P. Broecker and S. Trebst, Rényi entropies of interacting fermions from determinantal quantum Monte Carlo simulations, J. Stat. Mech.: Theory Exp. (2014) P08015.

[25] L. Wang and M. Troyer, Renyi entanglement entropy of interacting fermions calculated using the continuous-time quantum Monte Carlo method, Phys. Rev. Lett. **113**, 110401 (2014).

[26] F. F. Assaad, Stable quantum Monte Carlo simulations for entanglement spectra of interacting fermions, Phys. Rev. B **91**, 125146 (2015).

[27] J. D'Emidio, Entanglement entropy from nonequilibrium work, Phys. Rev. Lett. **124**, 110602 (2020).

[28] M. A. Metlitski, C. A. Fuertes, and S. Sachdev, Entanglement entropy in the $o(n)$ model, Phys. Rev. B **80**, 115122 (2009).

[29] S. Whitsitt, W. Witczak-Krempa, and S. Sachdev, Entanglement entropy of large-n wilson-fisher conformal field theory, Phys. Rev. B **95**, 045148 (2017).

[30] P. Zhang, C. Liu, and X. Chen, Subsystem Rényi entropy of thermal ensembles for SYK-like models, SciPost Phys. **8**, 094 (2020).

[31] P. Zhang, Entanglement entropy and its quench dynamics for pure states of the Sachdev-Ye-Kitaev model, J. High Energy Phys. 06 (2020) 143.

[32] P. Zhang, Quantum entanglement in the Sachdev—Ye—Kitaev model and its generalizations, Front. Phys. **17**, 43201 (2022).

[33] A. Chakraborty and R. Sensarma, Nonequilibrium dynamics of renyi entropy for bosonic many-particle systems, Phys. Rev. Lett. **127**, 200603 (2021).

[34] A. Haldar, S. Bera, and S. Banerjee, Rényi entanglement entropy of fermi and non-fermi liquids: Sachdev-Ye-Kitaev model and dynamical mean field theories, Phys. Rev. Res. **2**, 033505 (2020).

[35] S. Moitra and R. Sensarma, Entanglement entropy of fermions from wigner functions: Excited states and open quantum systems, Phys. Rev. B **102**, 184306 (2020).

[36] A. Chakraborty and R. Sensarma, Renyi entropy of interacting thermal bosons in the large-n approximation, Phys. Rev. A **104**, 032408 (2021).

[37] J. Hubbard, Electron correlations in narrow energy bands, Proc. R. Soc. London A **276**, 238 (1963).

[38] P. Fazekas, *Lecture Notes on Electron Correlation and Magnetism* (World Scientific, 1999).

[39] A. Auerbach, *Interacting Electrons and Quantum Magnetism* (Springer-Verlag, 1994).

[40] A. Georges, G. Kotliar, W. Krauth, and M. J. Rozenberg, Dynamical mean-field theory of strongly correlated fermion systems and the limit of infinite dimensions, Rev. Mod. Phys. **68**, 13 (1996).

[41] G. Kotliar, S. Y. Savrasov, K. Haule, V. S. Oudovenko, O. Parcollet, and C. A. Marianetti, Electronic structure calculations with dynamical mean-field theory, Rev. Mod. Phys. **78**, 865 (2006).

[42] H. Aoki, N. Tsuji, M. Eckstein, M. Kollar, T. Oka, and P. Werner, Nonequilibrium dynamical mean-field theory and its applications, Rev. Mod. Phys. **86**, 779 (2014).

[43] M. H. Hettler, M. Mukherjee, M. Jarrell, and H. R. Krishnamurthy, Dynamical cluster approximation: Nonlocal dynamics of correlated electron systems, Phys. Rev. B **61**, 12739 (2000).

[44] G. Kotliar, S. Y. Savrasov, G. Pálsson, and G. Biroli, Cellular dynamical mean field approach to strongly correlated systems, Phys. Rev. Lett. **87**, 186401 (2001).

[45] T. Maier, M. Jarrell, T. Pruschke, and M. H. Hettler, Quantum cluster theories, Rev. Mod. Phys. **77**, 1027 (2005).

[46] C. J. Bolech, S. S. Kancharla, and G. Kotliar, Cellular dynamical mean-field theory for the one-dimensional extended Hubbard model, Phys. Rev. B **67**, 075110 (2003).

[47] M. Capone, M. Civelli, S. S. Kancharla, C. Castellani, and G. Kotliar, Cluster-dynamical mean-field theory of the density-driven Mott transition in the one-dimensional Hubbard model, Phys. Rev. B **69**, 195105 (2004).

[48] E. Gull, A. J. Millis, A. I. Lichtenstein, A. N. Rubtsov, M. Troyer, and P. Werner, Continuous-time Monte Carlo methods for quantum impurity models, Rev. Mod. Phys. **83**, 349 (2011).

[49] S. Ryu and T. Takayanagi, Aspects of holographic entanglement entropy, J. High Energy Phys. 08 (2006) 045.

[50] W. Ding, A. Seidel, and K. Yang, Entanglement entropy of fermi liquids via multidimensional bosonization, Phys. Rev. X **2**, 011012 (2012).

[51] M. M. Wolf, F. Verstraete, M. B. Hastings, and J. I. Cirac, Area laws in quantum systems: Mutual information and correlations, Phys. Rev. Lett. **100**, 070502 (2008).

[52] M. Udagawa and Y. Motome, Entanglement spectrum in cluster dynamical mean-field theory, J. Stat. Mech.: Theory Exp. (2015) P01016.

[53] C. Walsh, P. Sémon, D. Poulin, G. Sordi, and A.-M. S. Tremblay, Local entanglement entropy and mutual information across the mott transition in the two-dimensional Hubbard model, Phys. Rev. Lett. **122**, 067203 (2019).

[54] C. Walsh, P. Sémon, D. Poulin, G. Sordi, and A.-M. S. Tremblay, Thermodynamic and information-theoretic description of the Mott transition in the two-dimensional Hubbard model, Phys. Rev. B **99**, 075122 (2019).

[55] C. Walsh, P. Sémon, D. Poulin, G. Sordi, and A.-M. S. Tremblay, Entanglement and classical correlations at the doping-driven mott transition in the two-dimensional hubbard model, PRX Quantum **1**, 020310 (2020).

[56] H. Park, K. Haule, and G. Kotliar, Cluster dynamical mean field theory of the Mott transition, Phys. Rev. Lett. **101**, 186403 (2008).

[57] W. Xu, K. Haule, and G. Kotliar, Hidden fermi liquid, scattering rate saturation, and nernst effect: A dynamical mean-field theory perspective, Phys. Rev. Lett. **111**, 036401 (2013).

[58] M. Raczkowski, R. Peters, T. T. Phùng, N. Takemori, F. F. Assaad, A. Honecker, and J. Vahedi, Hubbard model on the honeycomb lattice: From static and dynamical mean-field theories to lattice quantum Monte Carlo simulations, Phys. Rev. B **101**, 125103 (2020).

[59] J. Zang, J. Wang, J. Cano, A. Georges, and A. J. Millis, Dynamical mean-field theory of moiré bilayer transition metal dichalcogenides: Phase diagram, resistivity, and quantum criticality, Phys. Rev. X **12**, 021064 (2022).

[60] K. E. Cahill and R. J. Glauber, Density operators for fermions, Phys. Rev. A **59**, 1538 (1999).

[61] A. Altland and B. D Simons, *Condensed Matter Field Theory* (Cambridge University Press, 2010).

[62] A. L. Fetter and J. D. Walecka, *Quantum Theory of Many-Particle Systems* (McGraw-Hill, Boston, 1971).

[63] B. Kyung, G. Kotliar, and A.-M. S. Tremblay, Quantum monte carlo study of strongly correlated electrons: Cellular dynamical mean-field theory, Phys. Rev. B **73**, 205106 (2006).

[64] E. H. Lieb and F. Y. Wu, Absence of mott transition in an exact solution of the short-range, one-band model in one dimension, Phys. Rev. Lett. **20**, 1445 (1968).

[65] J. L. Cardy, *Scaling and Renormalization in Statistical Physics*, Cambridge Lecture Notes in Physics (Cambridge University Press, Cambridge, 1996).

[66] C. Holzhey, F. Larsen, and F. Wilczek, Geometric and renormalized entropy in conformal field theory, Nucl. Phys. B **424**, 443 (1994).

[67] G. Vidal, J. I. Latorre, E. Rico, and A. Kitaev, Entanglement in quantum critical phenomena, Phys. Rev. Lett. **90**, 227902 (2003).

[68] X. Chen, Y. Li, M. P. A. Fisher, and A. Lucas, Emergent conformal symmetry in nonunitary random dynamics of free fermions, Phys. Rev. Res. **2**, 033017 (2020).

[69] P. Calabrese, M. Mintchev, and E. Vicari, Entanglement entropies in free-fermion gases for arbitrary dimension, Europhys. Lett. **97**, 20009 (2012).

[70] H. Leschke, A. V. Sobolev, and W. Spitzer, Scaling of Rényi entanglement entropies of the free fermi-gas ground state: A rigorous proof, Phys. Rev. Lett. **112**, 160403 (2014).

[71] H. Widom, On a class of integral operators with discontinuous symbol, in *Toeplitz Centennial: Toeplitz Memorial Conference in Operator Theory, Dedicated to the 100th Anniversary of the Birth of Otto Toeplitz, Tel Aviv, May 11–15, 1981*, edited by I. Gohberg (Birkhäuser Basel, Basel, 1982) pp. 477–500.

[72] J. Shao, E.-A. Kim, F. D. M. Haldane, and E. H. Rezayi, Entanglement entropy of the $\nu = 1/2$ composite fermion non-fermi liquid state, Phys. Rev. Lett. **114**, 206402 (2015).

[73] W.-J. Hu, Y. Zhang, A. H. Nevidomskyy, E. Dagotto, Q. Si, and H.-H. Lai, Fractionalized excitations revealed by entanglement entropy, Phys. Rev. Lett. **124**, 237201 (2020).

[74] S. Banerjee, S. Bera, and A. Haldar (unpublished).

[75] B. Groisman, S. Popescu, and A. Winter, Quantum, classical, and total amount of correlations in a quantum state, Phys. Rev. A **72**, 032317 (2005).

[76] R. G. Melko, A. B. Kallin, and M. B. Hastings, Finite-size scaling of mutual information in monte carlo simulations: Application to the spin-$\frac{1}{2}xxz$ model, Phys. Rev. B **82**, 100409(R) (2010).

[77] R. R. P. Singh, M. B. Hastings, A. B. Kallin, and R. G. Melko, Finite-temperature critical behavior of mutual information, Phys. Rev. Lett. **106**, 135701 (2011).

[78] J. Iaconis, S. Inglis, A. B. Kallin, and R. G. Melko, Detecting classical phase transitions with renyi mutual information, Phys. Rev. B **87**, 195134 (2013).

[79] J.-M. Stéphan, S. Inglis, P. Fendley, and R. G. Melko, Geometric mutual information at classical critical points, Phys. Rev. Lett. **112**, 127204 (2014).

[80] G. Kotliar, E. Lange, and M. J. Rozenberg, Landau theory of the finite temperature Mott transition, Phys. Rev. Lett. **84**, 5180 (2000).

[81] M. O. Flynn, L.-H. Tang, A. Chandran, and C. R. Laumann, Momentum space entanglement of interacting fermions, Phys. Rev. B **107**, L081109 (2023).

[82] M. P. A. Fisher, V. Khemani, A. Nahum, and S. Vijay, Random quantum circuits, Ann. Rev. Cond. Matter Phys. **14**, 335 (2023).

[83] P. Calabrese, M. Campostrini, F. Essler, and B. Nienhuis, Parity effects in the scaling of block entanglement in gapless spin chains, Phys. Rev. Lett. **104**, 095701 (2010).

[84] B. Swingle, J. McMinis, and N. M. Tubman, Oscillating terms in the renyi entropy of fermi gases and liquids, Phys. Rev. B **87**, 235112 (2013).